Journal of Materials Chemistry A

ROYAL SOCIETY OF CHEMISTRY

REVIEW

View Article Online
View Journal | View Issue

Cite this: J. Mater. Chem. A, 2021, 9, 3180

Recent advances in highly active nanostructured NiFe LDH catalyst for electrochemical water splitting

Pradnya M. Bodhankar,[ab] Pradip B. Sarawade,*[ab] Gurwinder Singh,[c] Ajayan Vinu [c] and Dattatray S. Dhawale *[d]

Highly efficient, low-cost electrocatalysts having superior activity and stability are crucial for practical electrochemical water splitting, which involves hydrogen and oxygen evolution reactions (HER and OER). The sustainable production of hydrogen fuel from electrochemical water splitting requires the development of a highly efficient and stable electrocatalyst with low overpotential that drives electrochemical redox reactions. Electrochemical water splitting using highly active nickel-iron layered double hydroxide (NiFe LDH) catalyst having a very high turnover frequency and mass activity is considered as a potential contender in the area of electrocatalysis owing to the practical challenges including high efficiency and long durability at low overpotential, which shows great potential in future hydrogen economy. This review includes certain recommendations on enhancing the electrocatalytic performance of NiFe LDH-based electrocatalyst, particularly through morphology engineering, construction of hierarchical/core–shell nanostructures, and doping of heteroatoms through combined experimental assessment and theoretical investigations, which in turn improve the electrocatalytic performance. Finally, emphasis is made on the bifunctional activity of the NiFe LDH catalyst for overall water splitting. At the end, the conclusions and future outlook for the design of the NiFe LDH catalyst towards scale-up for their use as electrolyzer at the industrial level are also discussed.

Received 3rd November 2020
Accepted 9th December 2020

DOI: 10.1039/d0ta10712c

rsc.li/materials-a

[a]National Center for Nanosciences and Nanotechnology, University of Mumbai, Kalina, Mumbai-400098, India. E-mail: pradipsarawade@yahoo.co.in
[b]Department of Physics, University of Mumbai, Kalina, Mumbai-400098, India
[c]Global Innovative Centre for Advanced Nanomaterials, Faculty of Engineering and Built Environment, The University of Newcastle, University Drive, Callaghan, NSW 2308, Australia
[d]Qatar Environment and Energy Institute (QEERI), Hamad Bin Khalifa University (HBKU), Qatar Foundation, P. O. Box 34110, Doha, Qatar. E-mail: dattatraydhawale@gmail.com

Pradnya M. Bodhankar received her M.Phil degree in Nanosciences and Nanotechnology from the National Center of Nanosciences and Nanotechnology, University of Mumbai, India. She joined under Dr Pradip Sarawade's research group in July 2018 and is currently working on her Ph.D. thesis, which is focused on shape and size-controlled metal/metal oxide-based electrocatalysts for electrochemical water splitting. She is also working as a Woman Scientist (WOS-A) in the Department of Physics, University of Mumbai, under the grant received by the Department of Science and Technology (DST), India.

Dr. Pradip B. Sarawade is currently Assistant Professor at the Dept. of Physics, University of Mumbai, since September 2014. His research interest encompasses the development of nanomaterials with specific size and shape for energy and environmental applications. He has co-authored more than 60 peer-reviewed publications in high quality journals with citations more than 1500 with an h-index of 25 and 1 patent in the field of nanomaterials including a book on silica aerogels. He is a recognized Teacher at the University of Mumbai and guides students seeking M.Sc. (by research) and Ph.D degrees in the subjects of Physics, Chemistry, and Nanoscience and Nanotechnology.

1. Introduction

Currently, both energy crises and environmental pollution are the biggest concerns faced worldwide. Global energy demand is expected to grow from 16 Terawatt (TW) in 2010 to 23 TW in 2030 and 30 TW in 2050, which highlights the importance of clean and sustainable energy sources.[1,2] In this regard, hydrogen (H_2) production from electrochemical water splitting is a promising way to convert and use as a chemical fuel and provide renewable and clean energies. In particular, electrochemical water splitting through the electrolysis of water is considered as one of the most appropriate pathways for the sustainable production of hydrogen as a chemical fuel without generating any harmful byproducts.[3] Electrocatalytic two half-reactions oxygen evolution reaction (OER) and hydrogen evolution reaction (HER) are the vital steps in electrochemical water splitting and have been the subject of extensive study over the past decades. The thermodynamic potential of 1.23 V is the minimum requirement to drive the electrolytic cell for electrochemical water splitting corresponding to an energy input of $\Delta G = 273.1$ KJ mol^{-1} at standard temperature (25 °C) and pressure (1 atm).[4,5] Nevertheless, sluggish kinetics and consequently the large overpotential requirement toward both the reactions, *i.e.* OER and HER, become the main hindrances for the energy conversion processes as these would decrease the efficiency.[5,6] Noble-metal based electrocatalysts such as Pt for HER and RuO_2/IrO_2 for OER have shown the best performance toward electrochemical water splitting.[7–10] However, the low abundance, unaffordable cost (Pt = $ 861.82 ozt − 1, Ir = $ 1645.00 ozt − 1, Ru = $ 270.00 ozt − 1, InvestmentMine, Mining Markets & Investment, http://www.infomine.com/investment/metal-prices, accessed November 2020), and substandard stability of these noble metal-based electrocatalysts hinder large-scale H_2 production through water electrolysis.[11–13] Thus, it is of high importance to develop electrocatalysts for both HER and OER with low-cost, high earth-abundance, and those that can deliver the best performance. In an attempt to minimize the overpotential value and improve the efficiency of the overall water splitting process, many researchers have devoted their efforts on the selection and design of electrocatalyst materials. For instance, Wang *et al.*[14] conferred that the introduction of the carbon phase significantly enhances the electrical conductivity and the structure of the catalytic system. The HER catalytic performances of various non-noble metal-based carbon composites for a wide range of pH values have been reported.[14] The synergistic coupling of the carbon base and the active metal catalyst facilitates greater charge transfer and improves the activity.[14] Stable cobalt nanoparticle monolayer electrocatalyst for OER has also been studied.[15] Active OER catalysts from NiTi-LDH have been reported.[16] In addition, non-noble metal-based phosphides, sulfides, nitrides, borides, hydroxides, oxides, and LDHs (layered double hydroxides) have been extensively studied for OER, HER, and as bifunctional catalysts for overall electrochemical water splitting.[17–30] Amongst these active electrocatalysts, non-noble metal-based LDHs have attracted great attention and are considered as one of the most advanced electrocatalysts toward water splitting owing to their attractive physicochemical properties, flexible structural composition, variant synthetic technologies, and outstanding electrocatalytic activity.[31–34]

Dr. Gurwinder Singh is currently working as a senior researcher at the Global Innovative Centre for Advanced Nanomaterials (GICAN), the University of Newcastle, Australia. Dr Singh obtained his PhD in Materials Science under the supervision of Prof. Ajayan Vinu. His research is focused on the design and development of nanoporous carbon-based materials derived from biomass for CO_2 capture/conversion and energy storage.

Prof. Ajayan Vinu is a Global Innovation Chair Professor and the Director of Global Innovation Center for Advanced Nanomaterials (GICAN), the University of Newcastle. His research fields include advanced nanoporous materials and their applications in carbon capture and conversion, energy storage and conversion, adsorption and separation, as well as sensing and drug delivery systems. Prof. Vinu has published 410 papers in top-ranked journals, which has generated a high number of citations with an h-index of 74.

Dr. Dattatray S. Dhawale is a Scientist at the Qatar Environment and Energy Research Institute (QEERI), Qatar Foundation, Qatar since June 2016. His research interest encompasses the development of efficient nanomaterials for electrocatalysis, solar energy conversion, energy storage, photocatalysis, carbon capture and conversion, and sensors. He has co-authored more than 65 peer-reviewed publications in high-quality journals with ca. 3910 citations with an h-index of 36 and 4 patents in the field of energy technology.

Although different LDH-based catalysts, such as carbon/LDHs, cobalt–manganese LDH, cobalt–iron LDH, iron/aluminum LDHs, and nickel/iron-based LDHs have shown the best performance in energy storage and energy conversion applications,[35–44] NiFe LDH-based materials have attracted the greatest attention of the researchers owing to their excellent intrinsic activity as well as high catalytic durability. NiFe LDH displays superior performance towards electrochemical OER and HER compared to other transition metal-based catalysts and even noble catalysts such as RuO_2 and IrO_2.[28,45–49] Markovic *et al.*[50] established the trends in the activity of different types of 3d transition metal (oxy)hydroxides, particularly Ni, Co, Fe, and Mn for HER and OER. Their OER activities were determined to be in the order Ni > Co > Fe > Mn, which is in accordance with OH_{ad}–$M_{2+\delta}$. Boettcher *et al.*[51] found that $Ni_{0.9}Fe_{0.1}O_x$ is a more active OER catalyst than IrO_2 in the alkaline electrolyte. The *in situ* structural transformation from oxides to layered hydroxide/oxyhydroxides was observed for films containing Ni, which corresponds to the enhanced catalytic activity, revealing that Ni-based layered hydroxides/(oxy)hydroxides are the active catalysts.[51] Early reviews on this field are mainly focused on the structure, synthetic methods, mechanism, exfoliation, and energy-related applications of various LDH materials.[31,32,52–55] However, a review on the progress of LDH catalysts, especially NiFe LDH-based electrocatalysts for water splitting by covering the recent advancement in nanostructured designing strategies, trends in the fabrication processes, as well as the in-depth understanding of the mechanism, is urgently required. Thus, in this review, we emphasize the importance of NiFe LDH-based electrocatalysts for electrochemical water splitting. More specifically, this review includes certain recommendations for enhancing the electrocatalytic performance of NiFe LDH-based electrocatalysts, particularly through morphology engineering, constructing hierarchical/core–shell nanostructures, and doping heteroatoms. Finally, emphasis is made on the bifunctional activity of the NiFe LDH catalyst for overall water splitting. At the end, the conclusions and future outlook for the design of the NiFe LDH catalyst towards scale-up for its use as an electrolyzer at the industrial level is also discussed.

2. Salient features of NiFe LDH

LDHs are a class of 2D-layered materials that belong to the family of anionic clays or hydrotalcite-like compounds and were first established by Allmann and Taylor by employing the single crystal X-ray diffraction technique.[56–58] As depicted in Fig. 1, LDHs exhibit a layered-cluster structure, in which transition metals are positioned at the center of each octahedron and oxygen anions at the eight corners, which is represented as MO_6. The structure of LDH can be represented by the chemical formula $[M_{1-x}^{2+}M_x^{3+}(OH)_2]^{x+}[A_{x/n}^{n-}\cdot mH_2O]^{x-}$, where m is the interlayer water and $x = M^{3+}/(M^{2+}+M^{3+})$ is the layer charge density or the molar ratio.[59] M^{2+} are divalent cations (*e.g.*, Co^{2+}, Ni^{2+}, Zn^{2+}, Ca^{2+}, Mn^{2+}, Fe^{2+}, and Mg^{2+}) that are octahedrally coordinated to six OH^- hydroxyl groups and can be substituted by trivalent cations M^{3+} (*e.g.*, Al^{3+}, Ga^{3+} Fe^{3+}, Ti^{3+}, Cr^{3+}, In^{3+}) in the brucite-like $M^{2+}(OH)_2$ layer.[60,61] Such substitutions lead to the formation of positively charged layers, whose net charge is compensated. A^{n-} are the interlayer anions generally filled by CO_3^{2-}, which can be easily replaced by other anions (*e.g.*, NO^{3-}, SO_4^{2-}, ClO^{4-}, Cl^-, and Br^-).[62] The range $0.2 \leq x \leq 0.33$ is generally recognized as suitable for the synthesis of LDH compounds. The unique 2D-layered structure exhibited by LDH is appropriate for efficiently tuning the chemical and physical properties for their utilization in energy conversion and storage processes.[29,62–65] In case of NiFe LDH, when the Ni^{2+} ion is substituted by the Fe^{3+} ion, the brucite-type layered structure of β-$Ni(OH)_2$ is converted into an NiFe layer structure analogous to α-$Ni(OH)_2$.[39] The electrocatalytic performance of NiFe LDH can be enhanced with such a specific stacked-sheet-like architecture of the LDHs, which possesses adjustable exfoliation characteristics that can help to form ultrathin nanosheets that possess a high specific surface area, resulting in the exposure of more active sites.[66–68] In addition, the interlayer anion can be changed by the anion exchange process and the interlayer distance can also be varied. These features can efficiently modify the physicochemical properties of NiFe LDHs. The special electronic and lamellar architecture bestows NiFe LDH with an adequate specific surface area and excellent catalytic activity for electrochemical water splitting. Thus, NiFe LDH-based catalysts are more attractive because of the thin lamellar structure, tunable composition, and facile intercalation, resulting in excellent OER as well as HER performance. Han *et al.*[69] showed that the incorporation of molybdate ions as the charge-balancing species within the interlayers resulted in the formation of ultrathin NiFe LDH nanosheets. These ultrathin NiFe LDH nanosheets exhibited over four times higher density of electrochemically active sites and about three times larger OER current density as compared to regular NiFe LDH. Hunter *et al.*[49]

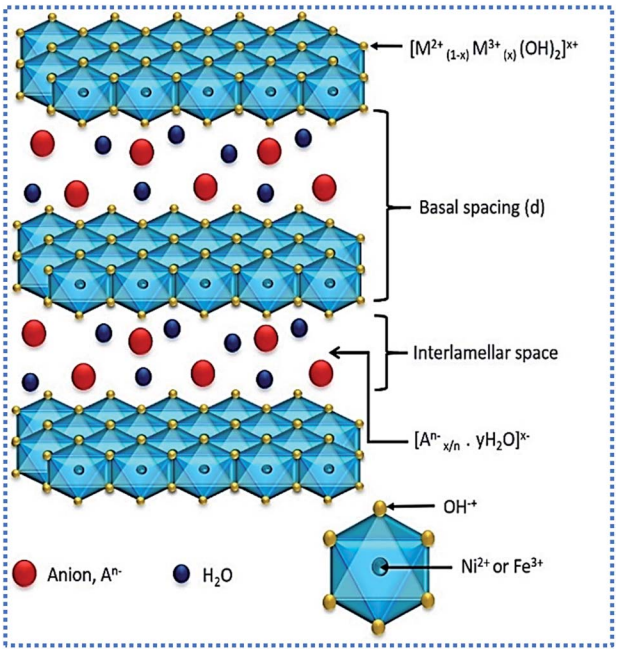

Fig. 1 The structure of the NiFe-layered double hydroxide.

reported that the water oxidation activity of the NiFe LDH catalyst can be tuned by incorporating anions with different basicitites and water oxidation mainly occurs on the nanosheet edges.

3. Fundamental mechanism of electrochemical water splitting

At present, there are several pathways for hydrogen production on a large scale, specifically, steam reforming of natural gas, coal gasification, steam-ion coal gasification, partial oxidation of heavy oil, catalytic decomposition of natural gas, and electrolysis of water.[70–76] Other methods, such as photochemical, photoelectron–chemical, photobiological, and thermochemical methods, are also being investigated.[77–80] Among all of these, water electrolysis is predominant in numerous ways.[3,70,81] Steam reforming of natural gas or hydrocarbons leads to the formation of a high content of carbonaceous material and also requires high temperature.[82,83] However, the use of high temperatures is a major drawback of the process.[84,85] Coal gasification is an alternative process of producing hydrogen at the industrial scale; however, high temperature (750 °C) and low pressure (<10 MPa) requirement, as well as the soil erosion and contamination problem, make it a disadvantageous method.[86] Unlike stream reformers, partial oxidation reformers are typically used to reform hydrocarbons such as gasoline, diesel, and heavy oil. These processes do not require catalysts and occur at a high-temperature range from 1150 °C to 1315 °C.[87] The main disadvantages of partial oxidation reformers include higher operating temperatures and pressures. Photoelectron–chemical water splitting is considered as an eco-friendly method for producing pure H_2. However, the H_2 production rate is poor and thus, despite being a greener method, it cannot be implemented for producing H_2 at a large scale.[88] Water electrolysis is a highly sustainable and eco-friendly way of producing pure H_2 at a large scale within short periods. Therefore, it is significant to define and discuss the details of fundamental electrochemistry and the mechanism involved in electrochemical water splitting, as given below.[89–91]

The water-splitting reaction expressed by eqn (1) consists of two half-reactions, namely, OER and HER, which occur on the anode and cathode, respectively. Following are the reactions that are proposed to be happening, depending on the reaction conditions.

$$H_2O \rightarrow H_2 + \frac{1}{2}O_2, \quad E^0 = 1.23 \text{ V} \tag{1}$$

In neutral condition:
At anode,

$$H_2O \rightarrow 2H^+ + \frac{1}{2}O_2 + 2e^-, \quad E^0 = -1.23 \text{ V} \tag{2}$$

At cathode,

$$2H_2O + 2e^- \rightarrow H_2 + 2OH^-, E^0 = 0.00 \text{ V} \tag{3}$$

In alkaline condition:
At anode,

$$2OH^- \rightarrow H_2O + \frac{1}{2}O_2 + 2e^-, \quad E^0 = -0.40 \text{ V} \tag{4}$$

At cathode,

$$2H_2O + 2e^- \rightarrow H_2 + 2OH^-, E^0 = 0.83 \text{ V} \tag{5}$$

In acidic condition:
At anode,

$$H_2O \rightarrow 2H^+ + \frac{1}{2}O_2 + 2e^-, \quad E^0 = -1.23 \text{ V} \tag{6}$$

At cathode,

$$2H^+ + 2e^- \rightarrow H_2, E^0 = 0.00 \text{ V} \tag{7}$$

3.1 OER mechanism

A number of the OER mechanisms have been reported and discussed in the existing literature.[92–96] OER is a four electron-proton coupled reaction, including multiple intermediates (eqn (8)–(17)) with O_2 produced from a combination of 2MO intermediates or the decomposition of MOH intermediates in both acidic and alkaline conditions, where M is a catalytically-active metal center.

In acidic condition:

$$M + H_2O \rightarrow MOH + H^+ + e^- \tag{8}$$

$$MOH \rightarrow MO + H^+ + e^- \tag{9}$$

$$MO + H_2O \rightarrow MOOH + H^+ + e^- \tag{10}$$

$$MOOH \rightarrow MO_2 + H^+ \tag{11}$$

$$MO_2 \rightarrow M + O_2 \tag{12}$$

In alkaline condition:

$$M + OH^- \rightarrow MOH + e^- \tag{13}$$

$$MOH + OH^- \rightarrow MO + H_2O + e^- \tag{14}$$

$$M + OH^- \rightarrow MOOH + e^- \tag{15}$$

$$MOOH + OH^- \rightarrow MO_2 + e^- \tag{16}$$

$$MO_2 \rightarrow M + O_2 \tag{17}$$

These reaction steps of OER in alkaline and acidic environment indicate the adsorption of H_2O and OH^- ion on the surface-active site M. This active site M undergoes a cycle of oxidation and reduction reactions during OER in both acidic and alkaline conditions with the evolution of the O_2 molecule and regenerates the fresh surface site for the next cycle. This

suggests that metals with variable and stable oxidation states can act as efficient electrocatalysts for OER. Thus, Ru and Ir for acidic and the hydroxides and oxides of Co, Ni, Fe, and Mn for alkaline conditions are considered as suitable electrocatalysts for OER.

3.2 HER Mechanism

HER usually involves three possible reaction steps in acidic and alkaline conditions.[97]

In acidic condition:

Volmer step:

$$H^+ + e^- + M \rightarrow MH_{ad} \quad (18)$$

Tafel step:

$$2MH_{ad} \rightarrow H_2 + 2M \quad (19)$$

Heyrovsky step:

$$H^+ + MH_{ad} + e^- \rightarrow H_2 + M \quad (20)$$

In alkaline condition:

Volmer step:

$$H_2O + e^- + M \rightarrow MH_{ad} + OH^- \quad (21)$$

Heyrovsky step:

$$MH_{ad} + H_2O + e^- \rightarrow H_2 + OH^- + M \quad (22)$$

Tafel step:

$$2MH_{ad} \rightarrow H_2 + 2M \quad (23)$$

where H_{ad} is the adsorbed hydrogen at the cathode.

As initially explained by Parsons *et al.*,[98] HER may occur *via* the Volmer–Heyrovsky mechanism or the Volmer–Tafel mechanism. In both the cases, hydrogen atoms are adsorbed at the electrode surface (H_{ad}) and the rate of the overall reaction is influenced by the free energy of hydrogen adsorption, ΔG_H.[98] The best HER catalysts should have hydrogen adsorption energies close to $\Delta G_H = 0$; bonding hydrogen too weakly or too strongly is not favorable.[99] Various materials have been investigated as active HER catalysts, including precious metals such as platinum,[99] metal phosphides,[100] metal borides,[101] metal oxides,[102] and metal sulfides.[103] It was found that Pt is a highly recognized HER catalyst in acidic environment owing to its great number of available active sites and optimum H-bonding strength.[99]

Fig. 2 shows the free energy diagram for the HER and OER reaction mechanism, which is constructed as a function of the applied electrode potential bias (E_1, E_2, and E_3), where the real catalyst denoted by blue lines indicates the identification of the rate-limiting steps in HER and OER electrocatalysis. The ideal catalyst is denoted by red lines for each of the aforementioned electrocatalysts (Fig. 2).[104] The red dashed trace in Fig. 2a indicates the Gibbs free energies of all the reactants and intermediates are equal at the equilibrium potential. The energetics of a real and ideal electrocatalyst at various electrode potentials for OER are displayed in Fig. 2b. It is inferred from Fig. 2b that the real OER electrocatalyst (blue) would need to shift the chemisorption free energy of the intermediates $OOH_{(ad)}$, $\Delta G_{OOH(ad)}$ to more negative values.[104]

3.3 Parameters for characterizing the electrochemical activity of OER and HER catalysts

To evaluate the catalytic activity of a given OER as well as HER electrocatalyst, few imperative parameters are required to be measured/calculated essentially. These mainly consist of overpotential at the benchmark current density of 10 mA cm^{-2}, Tafel slope, stability, turnover frequency (TOF), and mass activity.

(i) Overpotential at the Benchmark current density of 10 mA cm^{-2}

The water-splitting process through electrolysis requires potential greater than the thermodynamic voltage of 1.23 V to overcome the resistance. This additional voltage is termed as

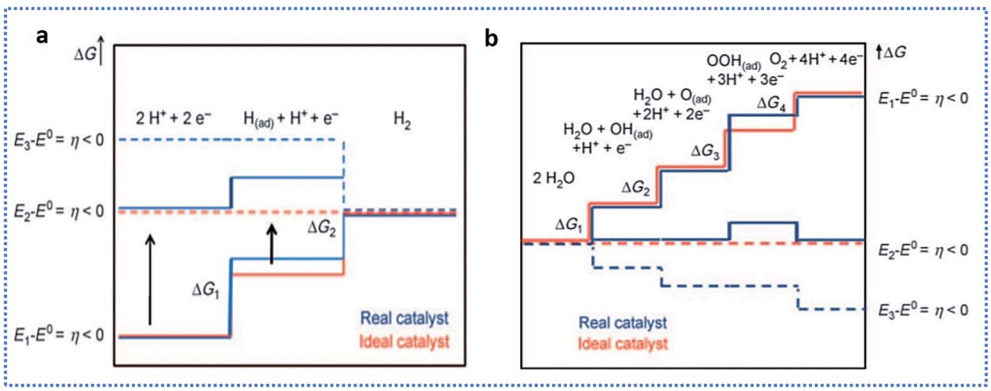

Fig. 2 Gibbs free energy diagram for the chemisorption of intermediates *versus* the reaction mechanism for (a) HER and (b) OER electrocatalysis. Blue and red refer to the real and the ideal reaction mechanism at three different electrode potentials (E_1, E_2, and E_3) respectively; the ideal reaction mechanism corresponds to an overpotential-free catalyst. The dashed line indicates energies at the electrode potential where all thermochemical barriers disappear. Reproduced with permission.[104] Copyright, 2010, WILEY VCH.

overpotential. For the electrocatalytic redox reaction, the applied potential can be expressed by the Nernst equation (eqn (24)).[105]

$$E = E^0 + \frac{RT}{nF}\ln\left(\frac{C_0}{C_R}\right) \quad (24)$$

where E is the applied potential, E^0 is the standard potential, R is the universal gas constant, T is the absolute temperature, F is the Faraday constant, and C_O and C_R are the concentrations of oxidized and reduced reagents, respectively.

Overpotential (η) can be represented as,

$$\eta = E - E_{eq} \quad (25)$$

where E_{eq} is the equilibrium potential. For water electrolysis, the overpotential (η) reported in the literature is at the benchmark current density of 10 mA cm^{-2}.

(ii) Tafel slope

The Tafel plot portrays the relation between steady-state current densities and overpotentials, which is represented by the Butler–Volmer equation.[106]

$$i = i_0\left[\exp\left(\alpha_a n\frac{FE}{RT}\right) + \exp\left(\alpha_c n\frac{F}{RT}\right)\right] \quad (26)$$

where i_0 is the exchange current density, and α_a and α_c are the symmetrical coefficients for the anode and cathode, respectively. The Tafel equation is given as

$$\eta = a + b\log(j) \quad (27)$$

where b is the Tafel slope.[107–109] From the Tafel equation, we can derive two important parameters, namely, theTafel slope (b) and exchange current density (j_0).

(iii) Electrochemically active surface area (ECSA)

The ECSA is determined using double layer capacitance (C_{dl}). First, multiple cyclic voltammetry (CV) scans are recorded in a non-faradaic region under a certain potential window at various scan rates (typically 10–200 mV s^{-1}). Then, the differences in the cathodic and anodic current density variation ($\Delta J = J_a - J_c$) at an overpotential are plotted against the scan rates and these plotted lines are fitted by linear regression, thus enabling the evaluation of double layer capacitance (C_{dl}). The slope of the fitted line is twice the value of C_{dl}. A high value of C_{dl} signifies large exposed surface active sites and higher current density.[110,111]

(iii) Turnover frequency (TOF)

The intrinsic catalytic activity of each catalytic site is evaluated by the TOF value. A high TOF value indicates an outstanding catalytic activity. The TOF is defined as the number of molecules that are catalytically generated per catalytic site per second and can be calculated by the following equation:

$$\mathrm{TOF} = \frac{(jA)}{(4Fn)} \quad (28)$$

where j is the current density at a constant overpotential, A is the area of the working electrode, F is the Faraday constant, and n is the number of moles of active materials.[31]

(iv) Stability

The robustness of the catalyst is determined by long-term stability testing. Good structural and catalytic stabilities of a catalyst are of crucial importance for a material that have some practical applications.

(v) Mass activity (MA)

In addition to the above-mentioned parameters, certain aspects such as the mass activity also define the quality of a catalyst and can be evaluated as

$$\text{Mass activity} = \frac{j}{m} \quad (29)$$

where j is the measured current density (mA cm^{-2}) and m is the mass loading (mg cm^{-2}) of the working electrode.[112]

4. Importance and role of Fe in the NiFe LDH catalyst in electrochemical water splitting

NiFe LDH-based catalysts have attracted attention in electrocatalysis because of their unique architecture, tunable configuration, and high specific surface area.[113–116] The unique 2D layered structure of NiFe LDHs has the advantage of interlayer-anion tunability, resulting in enhanced intrinsic activity.[40,49] Before getting into more discussions on the synthetic strategies, characterization techniques, theoretical investigation, and experimental details on NiFe LD- based electrocatalyst for water-splitting, it is vital to figure out the role of Fe active species in NiFe LDH.

In 1901, Edison and Junger[117] discovered the poisoning effect of Fe on the $Ni(OH)_2$ electrode while fabricating Ni-based alkaline battery. The study revealed that the decreased capacitance and cycle life resulted in improved OER performance by increasing the contamination *via* the Fe impurity. Later, in 1987, Corrigan *et al.*[118] for the first time presented the oxygen evolution performance of nickel oxide electrodes by the incorporation of Fe impurities. With only 0.01% of Fe doping, the OER overpotential was marginally lowered, indicating high sensitivity towards the OER activity of Fe-doped Ni-oxide electrode. With a greater percentage doping of Fe (>10%) into the Ni-oxide films, better electrocatalytic activities toward OER were observed (~200–250 mV overpotential at 10 mA cm^{-2} and a low Tafel slope of 20–25 mV dec^{-1}). Corrigan *et al.*[119] also studied the OER activity of $Ni(OH)_2$ films with other metal ions and compared it with that of co-deposited Fe/$Ni(OH)_2$. Recently, Gray *et al.*[120,121] reported that iron with a high oxidation state [*cis*-dioxo Fe(VI)] is the active site for the NiFe LDH catalyst in an alkaline water oxidation. Li *et al.*[122] also presented a critical review on Fe-containing electrocatalysts for OER. Nocera *et al.*[123] proposed that Fe^{3+} acts as a Lewis acid and advances the formation of Ni^{4+}. The presence of Fe in NiB_i films facilitates Ni^{4+} in the resting state of Ni oxide oxygen-evolving catalysts at modest overpotentials (350–250 mV). Smith *et al.*[124] reported the generation of negatively-charged surface sites ($NiOO^-$) in Ni-based oxygen evolution catalysts through the spectrochemical characterization of (Ni(Fe)OOH), which can be represented as

adsorbed "active oxygen". These active sites are generated due to the deprotonation process and this deprotonation effect in strongly alkaline electrolyte along with the Fe content has an important effect on the OER activity of nickel-based compounds. Strasser *et al.*[125] explored the role of Fe^{3+} in amorphous NiFe-based electrocatalysts. Under OER conditions in 0.1 M KOH, Ni atoms were present in the +4 oxidation state at Fe content < 4 at%. However, Ni atoms were stabilized the in low-valent +2 oxidation state at >4 the at% Fe content and thus the OER active state could be designated as $Ni^{+2}Fe^{+3}OOH$.[125] Zhao *et al.*[126] introduced Fe–O–Fe components in NiFe LDH by the partial substitution of Ni^{2+} with Fe^{2+} and these oxygen-bridged metal motifs played a crucial role in enhancing the OER activity (overpotential: 195 mV; current density: 10 mA cm^{-2}).

Edvinsson *et al.*[127] revealed a synergistic interplay between Fe and Ni in improving water electrolysis on the NiFeOOH catalyst. Fig. 3a shows the *in situ* Raman spectra, which shows Raman bands at 455 and 526 cm^{-1} during the HER process, indicating the metal oxygen vibrations for $Ni(OH)_2$ and FeOOH (Fe^{3+}), respectively. The HER mechanism on NiFe LDH is shown in the schematic illustration (Fig. 3b). Fig. 3b shows the formation of H_{ad} and OH_{ad} intermediates on the Ni^{2+} center (H_{ad}–NiO) and the Fe^{3+} center (OH_{ad}–FeO), respectively. In the case of OER, the authors suggest the potential dependent formation of FeOOH and NiOOH (Fig. 3c). It can be observed from Fig. 3d that the OH^- species tend to adsorb on the Ni^{2+} sites at higher overpotentials, forming OH_{ad} intermediate on the Ni site as the weaker interaction of OH^- with Ni^{2+} compared with Fe^{3+}. Fig. 3e represents the comparison of overpotentials of pristine NiFe LDH and dynamically self-optimized catalysts such as H–NiFe LDH and O–NiFe LDH obtained from the HER and OER polarization curves at the current density of 10 mA cm^{-2} without *iR* correction in 1 M KOH. It shows that the aged-NiFe LDH exhibited the lowest overpotential (243 mV) as compared to that of commercial Pt foil. Fig. 3f is the schematic illustration of the overall electrocatalytic working mechanism, indicating that the Ni and Fe species form the FeOOH and Ni–H intermediates under HER, while the γ-NiOOH intermediate is formed during OER, forming the synergistic effect and resulting in highly efficient bifunctional electrocatalyst.[127]

Boettcher *et al.*[46] studied the structure and activity of $Ni(OH)_2$, $Ni_{0.95}Fe_{0.05}(OH)_2$, and $Ni_{0.75}$ $Fe_{0.25}(OH)_2$ films as a function of aging in the electrolytes with varied impurities and showed that there is >30 fold increase in the conductivity of $Ni(OH)_2$/NiOOH when coprecipitated with Fe. At first, the as-deposited α-$Ni(OH)_2$ get converted into crystalline β-Ni(OH) during aging without application of a potential. The XRD analysis shows the appearance of new peaks (at $2\theta = 11°$ and 23.5°) after aging, which corresponds to mixed NiFe LDH. The CV scans (Fig. 4a and b) showed that the aging of $Ni(OH)_2$ in KOH with different purities has a direct effect on the shifting of the redox peaks to higher potentials with an increase in the OER activity. On the other hand, minute change was observed in the

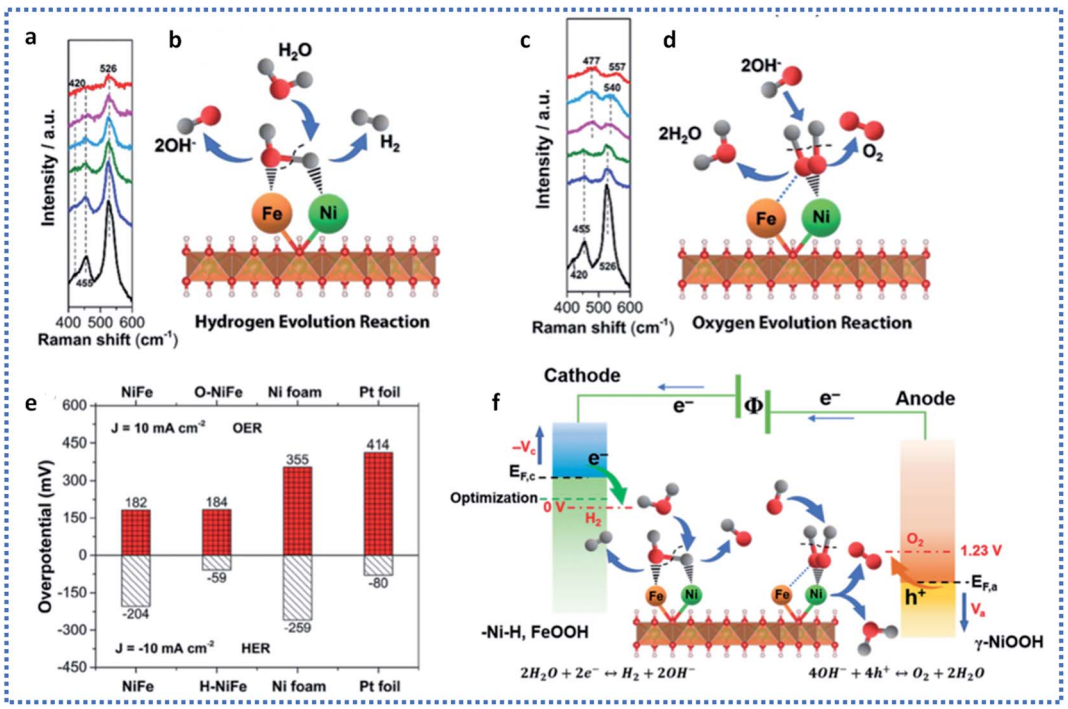

Fig. 3 (a and c) *In situ* Raman spectrum with 532 nm excitation under HER and OER condition, respectively. (b and d) Schematic illustration showing the reaction mechanism for HER and OER, respectively, on the NiFe LDH. (e) Overpotentials obtained from the OER and HER polarization curves of different catalysts at the current density of 10 mA cm^{-2} without *iR* correction in 1 M KOH aqueous electrolyte. (f) Graphical representation of the electrocatalytic generation of H_2 in 1 M KOH. Reproduced with permission.[127] Copyright 2019, the Royal Society of Chemistry.

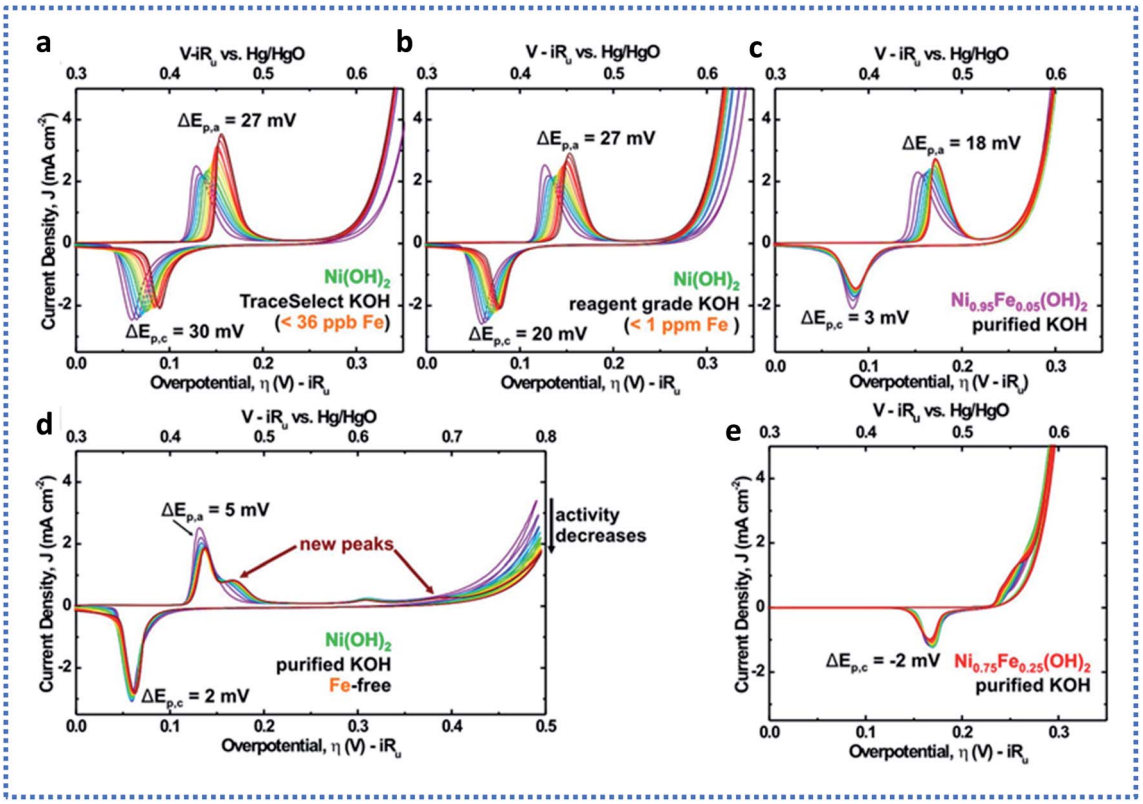

Fig. 4 (a, b and d) Cyclic voltammograms acquired during the aging of films with various purities of KOH. A total of 13 scans are shown for each sample; one for the initial as-deposited film (dark purple) and one additional scan after each 5 min aging period up to a total of 1 h of aging (dark red). (c and e) The changes in the anodic and cathodic wave positions ($\Delta E_{p,a}$ and $\Delta E_{p,c}$) are labelled for each set of CVs (no ΔE_p, the value is shown for the $Ni_{0.75}Fe_{0.25}(OH)_2$, as the oxidation wave is partially obscured by the OER current). Reproduced with permission.[46] Copyright 2014, American Chemistry Society.

electrochemical behavior for films with co-precipitated Fe in the purified electrolyte. Films with 5% ($Ni_{0.95}Fe_{0.05}(OH)_2$) or 25% ($Ni_{0.75}Fe_{0.25}OOH$) co-precipitated Fe does not show any remarkable change in the OER activity (Fig. 4c). However, the oxidation wave for the sample with 5% Fe shifts to a higher potential, indicating that the long-range order and inter-layer archive are insignificant for the active site OER activity. Fig. 4e represents the CV scans of the $Ni_{1-x}Fe_x(OH)_2$/$Ni_{1-x}Fe_x$-OOH films deposited on IDA electrodes.[46] Stahl *et al.*[128] implemented operando Mössbauer spectroscopic studies on a Ni : Fe layered hydroxide and hydrous Fe oxide electrocatalysts. The analysis evidenced Fe^{4+} ions in the Ni : Fe oxide catalyst during OER. The occurrence of Fe^{4+} in the NiFe catalyst is attributed to the stabilizing effect of the NiOOH lattice.[128] These results offer the importance of Fe and a unique insight into the synergistic roles of Ni and Fe in the NiFe LDH catalyst in electrochemical water splitting.

5. Design strategies for the NiFe LDH catalyst

To date, NiFe LDH electrocatalyst in the form of a powder or a thin-film has been fabricated by employing various physical and chemical routes such as pulsed laser deposition, hydrothermal/solvothermal, co-precipitation, and electrodeposition. Each of these synthetic methods has advantages over others. For instance, Hunter *et al.*[49,121] have fabricated the NiFe LDH material by using pulsed laser ablation in the liquid state and discussed the role of various inter-layer anions in enhancing the OER performance of NiFe LDH. The hydrothermal/solvothermal routes employed to obtain the nanostructure arrays/hierarchical structures of NiFe LDH offer control over the particle size, crystal structure, as well as growth dynamics.[39,40,129–136] The hybrid catalyst of NiFe LDH synthesized from the hydrothermal/solvothermal method has shown enhanced performance towards OER and HER as well as for overall water splitting.[137–140] Co-precipitation is the most frequent strategy used to prepare LDH in the variable as well as constant pH values. Valim *et al.*[141] compared the properties of various LDHs prepared by varying the pH values in the co-precipitation method. Liu *et al.*[142] prepared stable colloidal NiFe LDH nanoparticles by the facile and scalable co-precipitation method, which showed excellent water oxidation activity in the alkaline electrolyte with a high mass activity of 200 mA mg^{-1} at an overpotential of 260 mV and a low Tafel slope of 21.2 mV dec^{-1}. Besides the above-mentioned synthetic strategies, there are several other techniques that can be used to develop thin films of micro/nanostructured LDH. Some of these

techniques include chemical deposition, pyrolysis, and electrodeposition.[143,144] Among these, electrodeposition offers advantages such as low-cost, close connection, and fine electrical contact between the catalyst and the substrate.[145] By applying this method, not only the film thickness but also the composition and microstructure could be controlled by varying the bath composition, pH, bath temperature, and applied current density. This method has also been utilized in fabricating the NiFe LDH-based catalyst. Ren *et al.*[146] achieved excellent OER activity of the electrodeposited NiFe LDH nanosheets on nickel phosphide and established that the overall morphology and thickness of the nanosheets can be controlled by the electrodeposition time. When this electrodeposited NiFe LDH electrode was used for overall water splitting, the two-electrode cell was operated at 1.52 V to achieve current densities of 10 mA cm^{-2}, which was superior to the benchmark materials of IrO_2 and Pt.[146] Zheng *et al.*[147] constructed the core–shell heterostructure by growing the NiFe LDH film on CuO nanorod arrays, which were supported on Cu foil by applying the electrodeposition technique. The prepared electrocatalyst shows improved OER activity in 1 M KOH with a low overpotential of 290 mV at 50 mV cm^{-2} and displayed long term stability (35 h).

Apart from the synthetic strategies, the design of the working electrode also played a crucial role in enhancing the performance of water splitting. Various self-supported/binder-free NiFe LDH-based catalysts constructed on porous conductive substrates, such as Ni foam, Cu foil, and carbon cloth, have been utilized in electrochemical water splitting under low potential and show a large current density. For instance, Ding *et al.*[148] constructed NiFe LDH for OER and Cu_3P for HER on Cu weaving mesh. Remarkably, large stable current densities were obtained for both the OER (600 mA cm^{-2}) and HER (200 mA cm^{-2}) electrodes under low overpotential.[148] Sun *et al.*[149] demonstrated that the use of carbon cloth for amorphous NiFe-borate (NiFe–Bi) and layer formation on the NiFe-layered double hydroxide (NiFe LDH) surface greatly enhanced the OER activity with an overpotential of 294 mV to drive 50 mA cm^{-2} in 1 M KOH.

In addition to the use of different substrates, different strategies to modify the NiFe LDH catalyst that can improve its performance have also been applied. For instance, Hou *et al.*[150] prepared mesoporous nitrogen-doped NiFe layered double hydroxide/reduced graphene oxide (NiFe LDH/NrGO) nanospheres. The doping of *p*-CNNS resulted in superior ORR activity compared to pristine NiFe LDH and NiFe LDH/rGO.[150] Sun *et al.*[151] synthesized Ni foam-supported NiFe LDH nanoflakes array with a large electrochemically activated surface area, which exhibited a low overpotential of 245 mV at 10 mA cm^{-2} for OER. Guan *et al.*[152] demonstrated an *in situ* intercalation method to increase the interlayer spacing of the NiFe LDH electrode and this electrode required only 210 mV at 10 mA cm^{-2} overpotential to drive the OER. Li *et al.*[129] designed NiFe LDH on a 3D-graphene oxide matrix, which was embedded on Ni-foam as a substrate and succeeded in achieving an ultrasmall overpotential of 170 mV and a Tafel slope of 57 mV

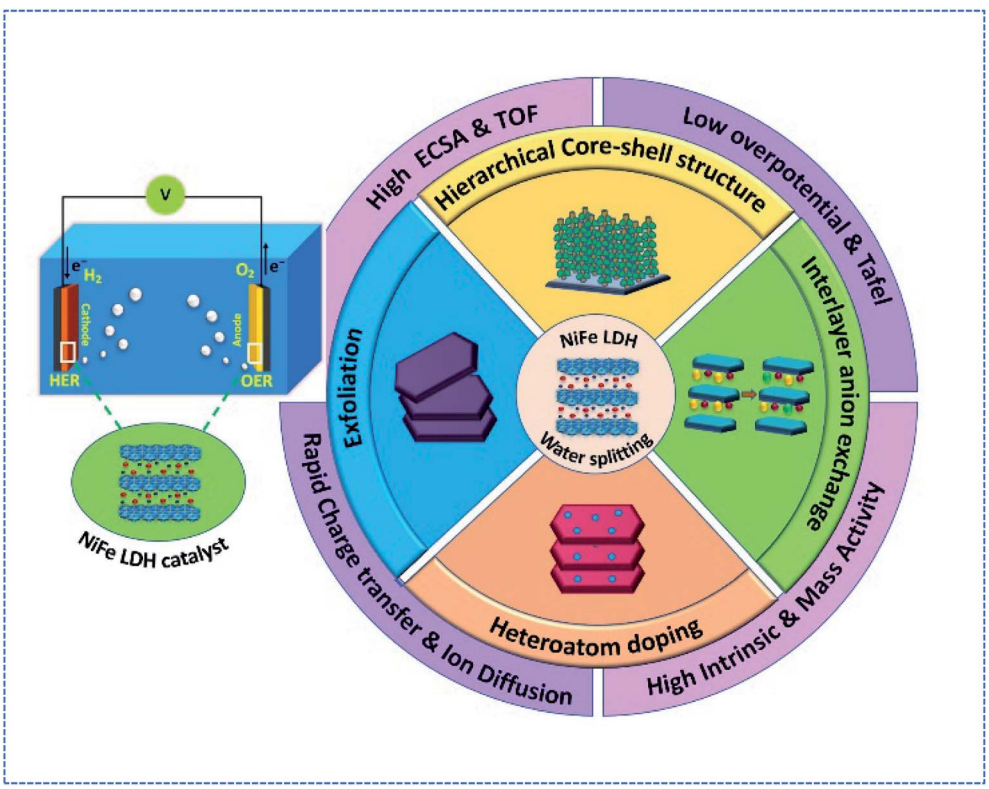

Fig. 5 Schematic showing different strategies in the design of nanostructured NiFe LDH-based electrocatalysts for water-splitting.

Table 1 Electrochemical parameters of the NiFe LDH-based electrocatalysts

Electrocatalyst	Morphology/method	Mass loading (mg cm^{-2})	Substrate (WE)/ electrolyte	η_{HER} (mV)@j (mA cm^{-2})/Tafel (mV dec^{-1})	η_{OER} (mV)@j (mA cm^{-2})/Tafel (mV dec^{-1})	Stability (h)	Ref.
NiFe LDHs	—/Hydrothermal	0.24 ± 0.3	CFP/1 M KOH	—	$300_{@10}$/36	—	40
NiFe LDH	Nanosheet/hydrothermal	—	NiFe alloy foam/1 M KOH	—	$233_{@30}$/38	5@370 mV	168
NiFe LDH	Nanosheets/coprecipitation	0.285	GC/1 M KOH	$116_{@10}$/74	$280_{@30}$/68	12@—	169
NiFe LDH	Nanosheets/hydrothermal	0.25	NF/CC/1 M KOH/PBS	—	$245_{@—}$/27	100@—	170
NiFe LDH	Nanoflakes/complexation-precipitation	—	Ni-foam/1 M KOH	—	$245_{@10}$/27	20@10 mA cm^{-2}	151
Fe–Ni LDH arrays	Nanosheets/hydrothermal	—	Ni-foam/1 M KOH	$127_{@10}$/109.4	$193_{@10}$/143.1	20@50 mA cm^{-2}	171
Monolayer NiFe LDH	Nanosheets/coprecipitation	0.35	Graphite paper/1 M KOH	—	$230_{@10}$/47	100@230 mV	172
DSO NiFe	Ultrathin layers/hydrothermal	—	Ni-foam	$59_{@10}$/62.3	$184_{@10}$/28.83	100@1.7 V	127
ORDE NiFe LDHs	Nanosheets/hydrothermal-exfoliation	—	Cu mesh/1 M KOH	—	$292_{@10}$/78.19	60@10 mA cm^{-2}	166
NiFe LDH HMS	Hollow spheres/coprecipitation	0.25	GCE & NF/1 M KOH	—	$300_{@71.69}$/53	11@300 mV	173
NiFe LDH microspheres	Microspheres/hydrothermal	0.1	GC/1 M KOH	—	$290_{@10}$/51	—	174
Au/NiFe LDH	Nanosheet/electrodeposition	2	Ti mesh/1 M KOH	—	$210_{@10}$/36	20@—	175
NiFe LDH@Au	Nanoarray/hydrothermal	—	Ni-foam/1 M KOH	—	$221_{@50}$/48.4	22@1.5 V	131
Ru-doped NiFe LDH	Nanosheets/hydrothermal	1.2	Ni-foam/1 M KOH	$29_{@10}$/31	$225_{@10}$/—	10@10 mA cm^{-2}	130
NiFeIr LDH	Nanosheets/hydrothermal	1.5	Ni-foam/1 M KOH	$34_{@10}$/32	$200_{@10}$/—	50@20 mA cm^{-2}	176
Pd–NiFe LDH	Sheet-assembled flower/electrodeposition	0.9	Ni-foam/1 M KOH	$130_{@10}$/46	$156_{@10}$/58	60@20 mA cm^{-2}	177
Ce-doped NiFe LDH	Nanoparticles/electrodeposition	0.8	Ni-foam/1 M KOH	$147_{@10}$/112	$175_{@10}$/59	40@20 mA cm^{-2}	178
NiCoFe LDH	Nanoarray/hydrothermal	—	Ni-foam/1 M KOH	—	$257_{@80}$/53	10@—	137
Co-modified NiFe LDH	Porous layers/hydrothermal	0.20	GC/1 M KOH	—	$265_{@10}$/47	24@1.5 V	132
Ag@NiFe LDHs	Nanowires/hydrothermal	0.224	Carbon paper/1 M KOH	$200_{@10}$/87	$330_{@10}$/89	12@10 mA cm^{-2}	140
3D core–shell Cu@NiFe LDH	Nanosheets/electrodeposition	2.2	Cu-foam/1 M KOH	$192_{@10}$/58.9	$199_{@10}$/27.8	48@10 mA cm^{-2}	179
NiFe LDH/CB	Nanosheets/hydrothermal	0.1	GC/1 M KOH	—	$220_{@10}$/35	12@10 mA/cm2	180
NiFe LDHs/NF@3D-rGO	Nanoflakes/hydrothermal	2.4	Ni-foam/1 M KOH	—	$170_{@20}$/57	24@10 mA/cm2	129
Carbon Quantum Dot/NiFe LDH	Nanoplate/coprecipitation-solvothermal	0.2	GC/1 M KOH	—	$235_{@10}$/10	8@2.5 mA cm^{-2}	181
NiFe LDH/NGF	Nanosheets/electrodeposition-hydrothermal	0.0207	Graphite foam/1 M KOH	—	—/57.9	12@1.47 V	182
Amorphous Ni_5P_4/NiP_2/NiFe LDH	Integrated 3D core–shell/electrodeposition	2.4	Ni-foam/1 M KOH	$95_{@10}$/—	$197_{@10}$/46.6	50@1.6 V	146
NiFeCe-LDH/CNT	Nanosheets/Nanocarbon/	0.2	GC/1 M KOH	—	$227_{@10}$/33	8@10 mA cm^{-2}	183

Table 1 (*Contd.*)

Electrocatalyst	Morphology/method	Mass loading (mg cm^{-2})	Substrate (WE)/ electrolyte	η_{HER} (mV)@j (mA cm^{-2})/Tafel (mV dec^{-1})	η_{OER} (mV)@j (mA cm^{-2})/Tafel (mV dec^{-1})	Stability (h)	Ref.
NiFe LDH/$NiCo_2O_4$	Hierarchical heterostructure/hydrothermal	4.9	Ni-foam/1 M KOH	$192_{@10}$/589	$290_{@50}$/—	12@20 mA cm^{-2}	133
NiFe LDH/CuO NRs/CS	Nanorods/electrochemical deposition	0.70	Cu foil/0.1 M KOH	—	$290_{@50}$/60	35@1.6 V	147
V–Ni_3S_2@NiFe LDH	Nanorods-nanosheets/hydrothermal-electrodeposition	—	Ni-foam/1 M KOH	—	$209_{@10}$/32.5	24@10 mA cm^{-2}	184
BA–NiFe LDHs/CP	Nanosheets/two-step hydrothermal	0.21	Carbon paper/1 M KOH	—	$203_{@10}$/50.9	20@—	185
NiFe LDH@NiCoP/NF	Nanowires/hydrothermal	2	Ni-foam//1 M KOH	$120_{@10}$/88.2	$220_{@10}$/48.6	100@10 mA cm^{-2}	135
NiO@NiFe LDH	Nanosheets on microflakes/hydrothermal	—	Ni-foam/1 M KOH	—	$265_{@10}$/72	50@50 mA cm^{-2}	186
NiFeLDH@NiFe–Bi/CC	Nanosheet/—	1.85	CC/1 M KOH	—	$294_{@50}$/96	20@—	149
GDY@NiFe LDH	Nanosheets/electrochemical deposition	1.03	Copper foil/1 M KOH	—	$260_{@10}$/95	6@1.52 V	187
GO-FeNi-LDH	Nanosheet arrays/electrochemical deposition	—	Ni-foam/1 M KOH	$119_{@10}$/36	$285_{@10}$/33	25@—	188
NiFe LDH@Ni_3S_2	Nanosheets/hydrothermal	—	Ni-foam/1 M KOH	$192_{@20}$/99	$230_{@50}$/29	12@10 mA cm^{-2}	189
GDY@NiFe LDH	3d/hydrothermal	—	Cu foam/1 M KOH	$163_{@10}$/106	$220_{@10}$/39.33	10@20 mA cm^{-2}	139
Ni_3Se_4@NiFe LDH/CFC	Micro/nanosheets/hydrothermal	—	CC/1 M KOH	$85_{@10}$/98.6	$223_{@10}$/55.5	100@10 mA cm^{-2}	190
$NiCo_2S_4$@NiFe LDH	Nanotubes@nanosheets/hydrothermal	—	Ni-foam/1 M KOH	$200_{@10}$/101.1	$201_{@60}$/46.3	12@10 mA cm^{-2}	138
NiFe LDH@Ni NTAs/NF	Nanotube arrays/electrodeposition	1.9	Ni-foam/1 M KOH	$101_{@50}$/101	$191_{@10}$/41	70@10 mA cm^{-2}	191
Co_3O_4@NiFe LDH	Nanosheets/hydrothermal	1.4	Ni-foam/1 M KOH	$74_{@50}$/107.5	$269_{@100}$/66	40@10 mA cm^{-2}	113
NiFe LDH@SWNT	Nanosheets/hydrothermal	0.272	GC/1 M KOH	—	$250_{@10}$/35	20@10 mA cm^{-2}	192
(Ni,Co)Se_2/NiFe LDH	Nanosheets on a Cactus-like/hydrothermal	—	CC/1 M KOH	—	$205_{@10}$/61	30@10 mA cm^{-2}	193
NiFe LDH/RGO	Platelike/solvothermal	0.5	Ni-foam/1 M KOH	—	$250_{@10}$/91	9@10 mA cm^{-2}	194
$NiFe_2O_4$/NiFe LDH	Nanoparticles/nanosheets/solvothermal	3	Ni-foam/1 M KOH	$101_{@10}$/67.1	$213_{@100}$/28.2	20@1.6 V	195
Cu_3P@NiFe LDH	Nanorod/solvothermal	—	CF/1 M KOH	—	$235_{@10}$/39	11@10 mA cm^{-2}	196
NiFe LDH/NrGO	Nanosphere/solvothermal	0.36	Ni-foam/0.1 M KOH	—	$250_{@10}$/63	9.5@0.5 V	150
NiFe LDH-NiSe	Nanosheets/hydrothermal	—	Ni-foam/1 M KOH	$276_{@100}$/70	$240_{@100}$/65.6	12@1.56 V	197

dec^{-1} at 20 mA cm^{-2}. These results show that the electrocatalytic performance of the NiFe LDHs can be improved by applying facile synthetic strategies, tuning of the structure, use of a conductive substrate, doping with different atoms in the host structure, and forming a hierarchical morphology, which assists in the formation of a large number of active sites and increase in the intrinsic catalytic activity, thereby making NiFe LDH highly efficient towards energy storage and conversion applications.

In the following sections, the review of different design strategies for the synthesis of NiFe LDHs such as nanostructuring, constructing hierarchical core–shell assembly, and heteroatom doping for their exploitation in improving the catalytic activity towards OER and HER are presented. Further, this review also presents the utilization of the NiFe LDH-based electrocatalyst in the high-performance electrolyzer and their scale-up industrial implementation. We summarized the most recent advancements in nanostructured NiFe LDH-based electrocatalysts for water splitting (Fig. 5 and Table 1).

5.1. Interlayer anion exchange of the NiFe LDH electrocatalyst

An early study revealed that the anion–exchange equilibrium constants for monovalent and divalent anions followed the sequence CO_3^{2-} > SO_4^{2-} > OH^- > F^- > Cl^- > I^- in the LDH, which exhibits a hydrotalcite-like structure.[153] The exchangeable charge-balancing interlayer anion property of the LDH makes it a potential candidate for electrocatalytic water splitting and is greatly dependent upon the CO_3^{2-} anions, which has a very strong affinity towards the LDH layers and can be delaminated.[63,154] However, these anions can be exchanged with other inorganic anions (Cl^-, SO_4^{2-}, *etc.*) or organic anions (acetate, lactate, dodecyl sulphate, *etc.*).[155,156] By incorporating multivalent non-noble transition metal ions into the 2D layered structure, different architectures could be built, which may open immense potential to design high-performance electrocatalysts at the nanoscales. In addition to inorganic and organic anions, reduced 2D graphene oxide (GO) nanosheets with atomic thickness, large surface area, and good electrical conductivity can also be used.[157,158] Yang *et al.*[157] have designed novel hybrid FeNi LDH with two types of oppositely charged nanosheets (cationic FeNi LDH and anionic GO). The group showed that the as-prepared FeNi-GO LDHs is a highly efficient electrocatalyst, which exhibits OER overpotential as low as 210 mV at 10 mA cm^{-2} and a Tafel slope of 40 mV dec^{-1}. Moreover, the reduced FeNi-GO LDH, denoted as FeNi-rGO LDH, shows further improvement in the OER activity with an overpotential of 195 mV at 10 mA cm^{-2} and the turnover frequency (TOF) of 0.98 s^{-1} was attained at the overpotential of 300 mV, indicating an outstanding OER catalyst. The intrinsic activity of FeNi LDH and facile charge transport through rGO led to the fine OER performance.[157]

Hunter *et al.*[49] fabricated NiFe LDH materials with distinct interlayer anions through anion exchange using pulsed laser ablation in liquid (PLAL). For the synthesis of anion-exchanged NiFe LDH, a combination of different nickel salts (sulphate/chloride and nitrate) are used to prepare the nickel precursor [NiFe]–$(NO_3^-)^-$ solution and irradiated for 60 min with the help of the Nd:YAG laser, followed by unreacted iron ablation target using a rare-earth magnet. Anion exchange was achieved by suspending a given amount of the [NiFe]–$(NO_3^-)^-$ LDH nanosheets in aqueous alkali salt solutions of K_2CO_3, KOH, KCl, NaF,

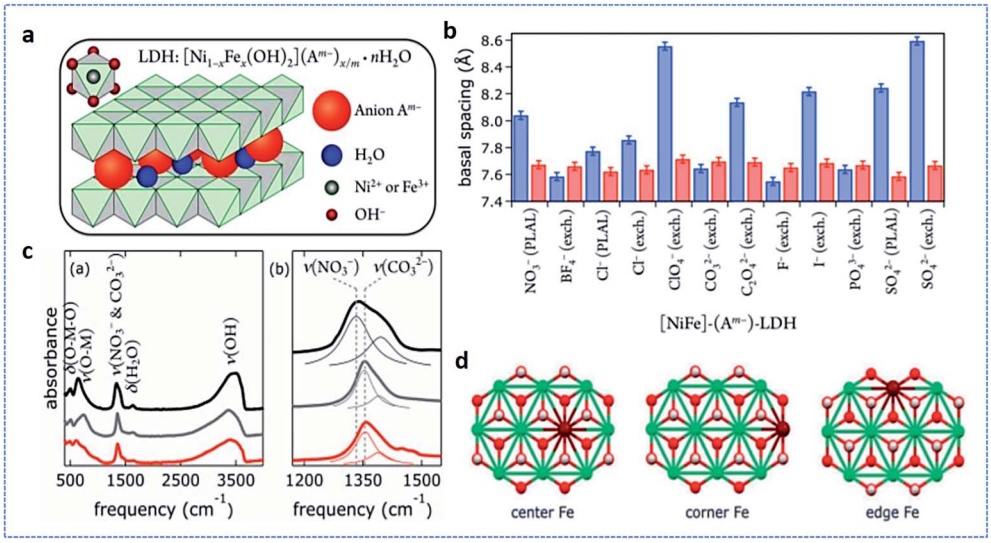

Fig. 6 (a) Schematic illustration of the NiFe LDH structure. The anions and water are present in the interlayer space, and Ni^{2+} or Fe^{3+} ions are surrounded by six hydroxides in distorted octahedral coordination (upper left). (b) The basal spacing of the NiFe LDH nanosheets with different interlayer anions as synthesized (blue) and after suspension in 1.0 M aqueous KOH in ambient air (red). (c) Infrared spectra of [NiFe]–(NO^{3-})-LDH nanosheets as synthesized (black), after being suspended in 0.1 M aqueous K_2CO_3 solution (grey), and after being suspended in 0.1 M aqueous KOH (red); (a) full spectra, (b) magnification of the region characteristic for NO^{3-} and CO^{3-}, Lorentzian fits are depicted as thin lines. (d) Fe sites in the basic $[Ni_9Fe_1(OH)_{18}]^{3+}$ cluster fragment; Ni: green, Fe: maroon, O: red, and H: white. Reproduced with permission.[49] Copyright 2016, the Royal Society of Chemistry.

Na_2SO_4, $NaClO_4 \cdot 1H_2O$, KI, KBF_4, K_3PO_4, and $K_2C_2O_4 \cdot 1H_2O$. Fig. 6a shows the schematic design of the anion-exchanged NiFe LDH structure. Divalent nickel cations (Ni^{2+}) or trivalent iron cations (Fe^{3+}) are surrounded by six hydroxides (OH^-) in distorted octahedral coordination, and water and anions occupy the interlayer space, as shown in the inset of Fig. 6a. The basal spacings of the NiFe LDH nanosheets were calculated from Gaussian fits of the (003) peaks and the angle of incidence was obtained for different interlayer anions. The calculated basal spacings of the [NiFe]–(Am^-)–LDH materials with different intercalated anions Am^-, prepared by PLAL or by anion exchange from [NiFe]–(NO_3^-)$^-$ LDH (exch.), is depicted in Fig. 6b, which shows that the basal spacings of NiFe LDH materials were correlated with the ionic radii of the anions. This indicated that the anions can be present in the interlayer arcades of LDH materials. Successful interlayer anion exchange in NiFe LDH ([NiFe]–(NO_3^-)$^-$ LDH into [NiFe]–(CO_3^{2-})$^-$ LDH) in 1 M KOH in ambient air is evident from the infrared (IR) spectra (Fig. 6c). The de-carbonation of the catalyst was achieved by the precipitation of dissolved carbonate with Ba^{2+} as $BaCO_3$ in Ar atmosphere using $Ba(OH)_2$. The characteristic redshift and broadening of the nitrate, as compared to carbonate shown by IR spectrum, indicated that the carbonate-free [NiFe]–(NO_3^-)$^-$ LDH catalyst and the electrolyte were successfully obtained. Both the catalysts (carbonate ion-containing and carbonate ion-free) were tested for OER, wherein the [NiFe]–(CO_3^{2-})$^-$ LDH catalyst showed better performance as compared to [NiFe]–(NO_3^-)$^-$ LDH, displaying the effect of interlayer anions during water oxidation catalysis. The assessment with the model cluster (Fig. 6d) indicates the binding of nitrate and nitrite ions to different Fe sites. Similarly, the DFT calculations of [$Ni_9Fe_1(OH)_{20}(NO_{2or3})$] suggest that higher water oxidation activity depends on nitrite bound by its N-atom to the edge-site iron. This result indicates that iron sites on the edges of the NiFe LDH nanosheets are highly active in water oxidation catalysis.[49]

5.2. Exfoliation/intercalation of the NiFe LDH catalyst

The exfoliation/intercalation of bulk LDH into ultrathin LDH is an efficient strategy to modify the LDHs, by which it can be directly utilized in the energy conversion applications due to increased surface area, exposure of rich active sites, and abundant defects.[33,159,160] The exfoliation of LDH materials is a two-step process; in the first step, the interlayer distance is increased by intercalating the LDH material and in the second step, the layers are delaminated using various techniques. There are several approaches reported for the exfoliation of LDH such as laser ablation, electrostatic repulsion, using polar as well as non-polar solvents, and mechanical forces.[161–165]

Hu *et al.*[45] for the first time established that the liquid-phase exfoliated single-layer nanosheets (size: 200–500 nm) of NiFe and NiCo LDHs are highly active electrocatalysts for OER. A hydrothermal process (150 °C, 2 days), followed by inter-layer anion exchange, was carried out to prepare NiFe, NiCo, and CoCo LDHs. The prepared powder (NiFe LDH-ClO_4) was dispersed in degassed formamide, followed by sonication and mechanical stirring under N_2 atmosphere (24 h) and irradiation with a laser beam, which assisted with the exfoliation of the single LDH layers (Fig. 7a). The obtained 0.8 nm thick nanosheet was confirmed by XRD. In 1 M KOH, the significantly higher OER catalytic activity of the single-layer nanosheets was observed at a current density of 10 mA cm^{-2} as compared with the bulk LDHs, which was due to the increase in the active site density and conductivity (Fig. 7b). Among the three LDHs examined for OER, the catalytic activity followed the order NiFe > NiCo > CoCo for both the exfoliated nanosheets and bulk LDHs.[45]

Guan *et al.*[152] implemented the *in situ* intercalation strategy on electrodeposited NiFe LDH to increase the interlayer spacing of LDH. To prepare the catalyst, the NiFe LDH electrode was first immersed in formamide at a pre-set temperature of 80 °C for 3 h duration and the interlayer spacing was found to increase from 7.8 to 9.5 Å. The NiFe LDH material was grown on the carbon rod by applying a unipolar pulse electrodeposition method, followed by *in situ* intercalation to increase the interlayer spacing of electrodeposited NiFe LDH. The electrode required only 210 eV overpotential to reach the current density of 10 mA cm^{-2}. Further, when ultrasound treatment was given to the NiFe LDH electrode, the intercalation time was reduced and the overpotential for OER decreased to 203 mV at 10 mA cm^{-2}. The schematic diagram is shown in Fig. 7c. The intercalated NiFe LDH electrode exhibited low ohmic and charge transfer resistances, indicating good conductivity. The prepared catalyst also possessed high TOF (0.086 s^{-1}) and showed stable long-term performance (18 h).[152]

Moreover, Yong *et al.*[166] fabricated *in situ* surfactant-free exfoliated NiFe LDH by thermodynamically-driven Ostwald ripening, followed by redeposition through a facile hydrothermal treatment. Fig. 7d depicts the systematic synthetic procedure of Ostwald ripening driven exfoliation (ORDE) of NiFe LDH. An increase in the self-etching duration during the exfoliation of bulk NiFe LDH results in a decrease in the average thickness of the nanosheets. Fig. 7e and f show the SEM images of the vertically-aligned bulk NiFe LDH nanosheets on the Cu mesh and exfoliated NiFe LDH after 8 h hydrothermal treatment, respectively. The prepared NiFe nanosheets exhibited higher electrochemical active surface area and ample exposed active edges and sites, which in turn established significantly enhanced OER performance with a low overpotential of 292 mV at 10 mA cm^{-2} and long-term stability for more than 60 h, as well as remarkable flexibility.[166]

Recently, Zhao *et al.*[167] have obtained monolayer nanosheets of NiFe LDH and graphene oxide (GO) by applying solid-phase exfoliation strategy. The group discovered that a dynamic evolution process could exist between the NiFe LDH nanosheets (NiFe LDH-NS) and GO nanosheets (GO-NS) to assemble a new NiFe LDH/GO (NFGO) nanohybrids, *i.e.*, well-organized NiFe LDH-NS standing on GO-NS. NiFe LDH was prepared by a hydrothermal method, GO by a modified Hummers' method, and polyhydroxy material is used as an exfoliated material for the exfoliation of NiFe LDH and GO. The floclike-precipitated NFGO nanohybrids were obtained by dispersing NiFe LDH-NS in the solution and self-assembled with GO-NS. The obtained

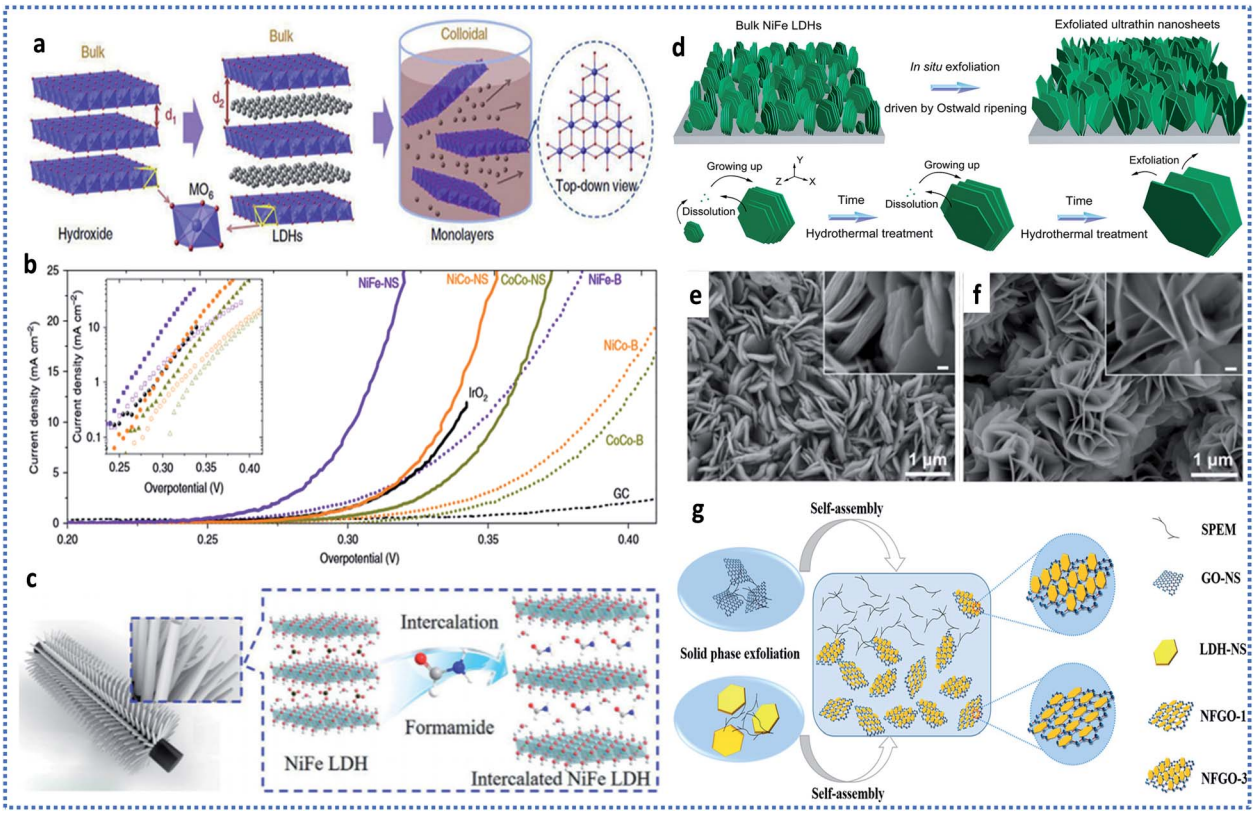

Fig. 7 (a) Schematic representation of the materials' structures. Layered hydroxides, d_1 is the inter-layer distance. LDH with inter-layer anions and water molecules, d_2 is the inter-layer distance, $d_2 > d_1$. Exfoliated LDH monolayers dispersed in a colloidal solution. Every single layer is composed of edge-sharing octahedral MO_6 moieties (M denotes a metal element). (b) The electrochemical behavior of LDH materials and IrO_2 nanoparticles in 1 M KOH. Polarization curves. Inset shows the Tafel plots (scan rate: 5 mV s^{-1}). Reproduced with permission.[45] Copyright 2014, Nature Publishing Group. (c) Schematic diagram of the *in situ* intercalation process over the electrodeposited NiFe LDH nanosheets on a substrate. Reproduced with permission.[152] Copyright 2017, Elsevier. (d) Schematic for the ORDE of pristine bulk NiFe LDHs into exfoliated ultrathin nanosheets. SEM characterization of (e) pristine bulk and (f) exfoliated NiFe LDHs for 8 h. Insets: the corresponding enlarged views. Reproduced with permission.[166] Copyright 2018, American Chemistry Society. (g) Scheme for the preparation of NiFe LDH/GO nanohybrids based on the solid-phase exfoliation-liquid-phase assembly strategy. Reproduced with permission.[167] Copyright 2019, American Chemistry Society.

NFGO nanohybrids were then reduced to form the NiFe LDH/RGO (NFRG) nanohybrids (Fig. 7g). NFRG-3 shows excellent performance towards OER with an overpotential of 273 mV at 30 mA cm^{-2}. Reduced graphene oxide (rGO) plays a dominant role in improving the conductivity, charge transfer efficiency, and synergistically-improved OER activity of nanocomposites.[167]

Ma *et al.*[158] constructed the superlattice structure composed of $Ni_{2/3}Fe_{1/3}$ LDH nanosheets and reduced GO by the exfoliation method. The heterostructure exhibited excellent OER performance in 1 M KOH solution with a low overpotential (230 mV) and Tafel slope (42 mV dec^{-1}). The improvement in the activity was further observed (overpotential of 210 mV at 10 mA cm^{-2} and Tafel plot of 40 mV dec^{-1}) when the combination of $Ni_{2/3}Fe_{1/3}$ LDH nanosheets and the conductive rGO($Ni_{2/3}Fe_{1/3}$r-GO) was catalyzed for OER.[158] Furthermore, Yao *et al.*[66] demonstrated heterostructured NiFe LDH-NS@DG10 hybrid catalyst coupled with exfoliated NiFe LDH nanosheets (NS) and defective graphene (DG). The hybrid catalyst displayed enormously high electrocatalytic activity for OER and HER in 1 M KOH with an overpotential of 210 mV and 115 mV, respectively, at 10 mA cm^{-2}. The catalyst, when operated in the bifunctional mode, achieved a current density of 20 mA cm^{-2} with a cell voltage requirement of only 1.5 V.[66]

5.3. Hierarchical/core–shell nanostructure of the NiFe LDH electrocatalyst

In an attempt to optimize and improve the OER and HER performance of NiFe LDH catalysts, various approaches have recently been explored to specifically synthesize NiFe LDH catalysts at the nanoscale.[170,172,198,199] Since water electrolysis always occurs on the surface of the catalyst, designing a nanostructured catalyst is an effective strategy to increase the surface area significantly. The nanostructured catalyst has more active sites per geometric area, which facilitates the diffusion of ions through the electrolyte and enhances the chemical activity during electrocatalytic water splitting.[16,200,201] Liu *et al.*[170] demonstrated that bulk NiFe LDH becomes unstable during OER. The group has grown NiFe LDH on Ni foam or carbon cloth and investigated the deactivation mechanism of LDH in OER. Fig. 8a is the schematic illustration displaying NiFe LDH

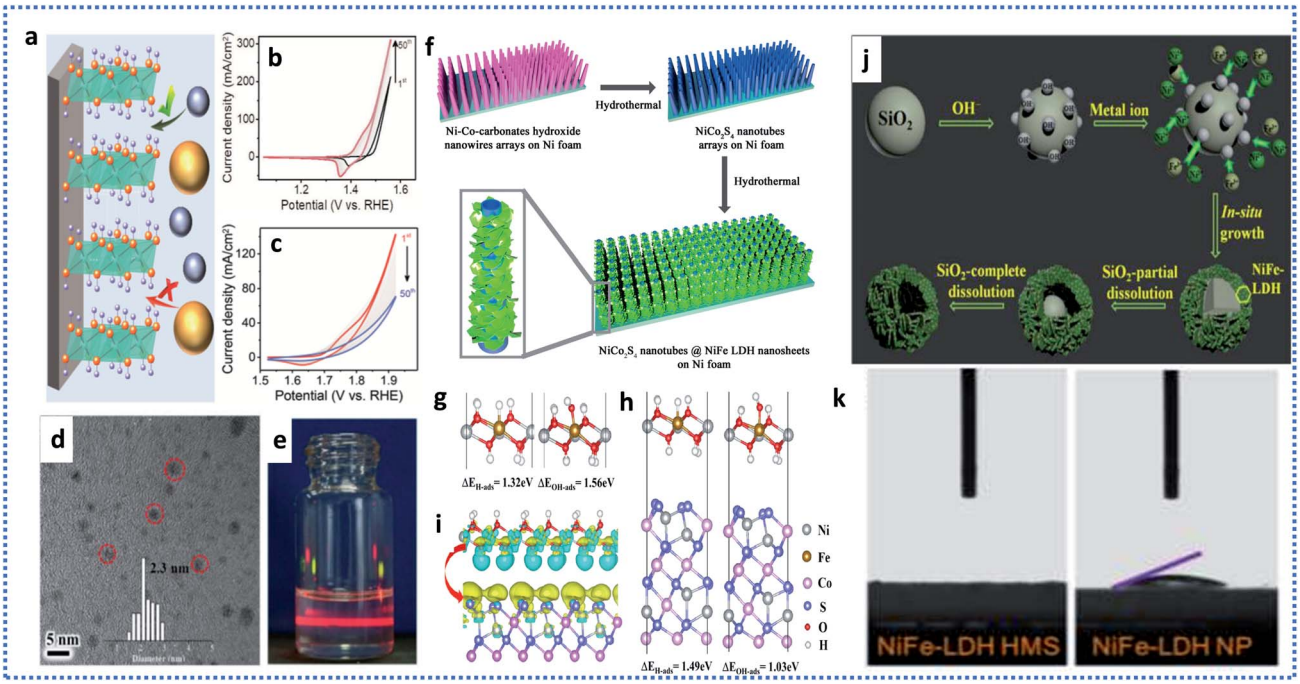

Fig. 8 (a) Schematic illustration showing NiFe LDH on the substrate with different accessibility to proton acceptors. (b) The CV curves of NiFe LDH on Ni foam recorded at a scan rate of 10 mV s^{-1} (without *iR* correction, $R_s = 0.28\ \Omega$). (c) CV curves recorded in 1 M PBS ($R_s = 0.5\ \Omega$). Reproduced with permission.[170] Copyright 2019, WILEY-VCH. (d) High-angle annular dark-field HRTEM of LDH-UF. (e) A dispersion of the ultrafine LDH nanosheets in ethanol displaying Tyndall effect. Reproduced with permission.[202] Copyright 2018, WILEY-VCH. (f) Schematic illustration of the synthetic process of $NiCo_2S_4$@NiFe LDH/NF heterostructures. Adsorption geometries of the intermediates *H and *OH on the surfaces of (g) NiFe LDH and (h) $NiCo_2S_4$@NiFe LDH/NF heterostructures, respectively. (i) Interfacial electron transfer between $NiCo_2S_4$ and NiFe LDH. Reproduced with permission.[138] Copyright 2017, American Chemistry Society. (j) Scheme of synthesis of NiFe LDH HMS. (k) Contact angle test over NiFe LDH HMS and NiFe LDH NP. Reproduced with permission.[173] Copyright 2016, American Chemistry Society.

on the substrate with different accessibility to proton acceptors. Electrolysis was performed in 1 M KOH (Fig. 8b) and 1 M phosphate buffer saline (Fig. 8c) to reveal the number of active sites during repeated CV scans. The authors propose that the delamination of multi-layered NiFe LDH into atomically thin nanosheets effectively improved the OER and stability of the NiFe LDH. The Tafel plots of the first and 50th CV curves were found to be nearly identical with the values of 24 mV dec^{-1} and 27 mV dec^{-1}, respectively, despite the different catalytic activity, suggesting that improved activity may originate from an increased number of active sites.[170]

Recently, Zhang *et al.*[202] reported the successful synthesis of ultrafine NiFe LDH nanosheets with size less than 3.0 nm. The HR-TEM image (Fig. 8d, inset particle size distribution) shows LDH-ultrafine with a mean particle size of 2.3 nm. Fig. 8e displays a dispersion of the ultrafine LDH nanosheets in ethanol, representing the Tyndall effect. These ultrafine nanosheets encompassed an abundance of anion and cation vacancies due to their small size and thus offered excellent OER activity.[202] Wang *et al.*[203] successfully fabricated NiFe-based LDH with a laminar structure (denoted as NFLS) by employing a one-step hydrothermal method and sodium dodecyl sulphate as the surfactant. The as-prepared NFLS exhibited a well-defined periodic layered-stacking geometry (1.0 nm) and displayed an outstanding OER activity with an overpotential of 197 mV at the current density of 10 mA cm^{-2}.[203] Luo *et al.*[204] synthesized 3D NiFe LDH nanosheet arrays, which were vertically aligned on free-standing nitrogen-doped graphite foam (NGF). The hybrid catalyst exhibited a low onset overpotential of 233 mV in 1 M KOH. Superior electrochemical performance was attributed to the binder-free approach, which could provide more electrochemical active sites and facilitate the transportation of the electrolyte and the gas product.[204]

The fabrication of a catalyst with hierarchical nanostructure can provide abundant active sites and facilitate ion transport kinetics, which enhances the activity and stability for water splitting. Moreover, the utilization of hierarchical nanostructures can offer numerous other advantages, such as facilitating the electrolyte penetration and accelerating the bubble release rate by providing the larger free space.[205]

Another strategy used by researchers to improve the performance of the electrocatalyst in water splitting is constructing nano-sized core–shell structure. Core–shell organized NiFe LDH-based electrocatalysts are exceptional as they represent the combination of individual components into a useful framework, showing enhanced physical and chemical properties, which are unobtainable from the individual components. Further, core–shell nanostructures could improve the catalytic activity and durability for water splitting by facilitating mass transport, altering the electronic structure, exposing large active sites, and modifying the surface reactivity.[206] The strategy of surface engineering of electrode materials for water splitting by

constructing nickel–iron ($Ni_{0.95}Fe_{0.05}$) layered double hydroxide nanosheets (LDH) on silver nanowires (Ag NWs) was reported by Chu *et al.*[140] The hierarchical core–shell architecture was designed by using nanosized Ag as a conductive support. The exceptionally high conductivity of Ag enhanced the electron transport as compared to pure carbon. The support-catalyst contact area was also improved. The high stability and excellent mass transfer for the escape of oxygen bubbles were also shown by the same catalyst. The hierarchically constructed Ag nanowires@NiFe LDH nanostructures for electrocatalytic water splitting showed excellent activity both in cathodic and anodic processes, which required a small cell potential of 1.56 V so as to achieve a current density of 10 mA cm^{-2}.

Jiang *et al.*[138] devoted the efforts to engineer $NiCo_2S_4$@NiFe LDH heterostructures. The first-principles calculation based on density functional theory displayed strong interaction and charge transfer between $NiCo_2S_4$ and NiFe LDH, which altered the interfacial electronic structure and surface reactivity (Fig. 8g–i). In the synthesis, firstly, the $NiCo_2S_4$ nanotube arrays were prepared on Ni foam by a three-step hydrothermal method. Then, the $NiCo_2S_4$@NiFe LDH/NF heterostructures were obtained by immersing the prepared $NiCo_2S_4$ nanotube array in the solution of nickel and iron precursors and the reaction was carried for 10 h at 120 °C. The schematic of the preparation of the $NiCo_2S_4$@NiFe LDH/NF heterostructure is shown in Fig. 8f. The prepared catalyst exhibited the improved performance for OER with a low overpotential of 201 mV at the current density of 60 mA cm^{-2} and low Tafel slope of 46.3 mV dec^{-1}. The catalyst also acted as a bifunctional candidate with the requirement of cell potential of 1.6 V so as to reach 10 mA cm^{-2} for the overall water splitting process.[138]

Wei *et al.*[173] in their electrochemical studies of the NiFe LDH hollow microspheres (HMS) revealed that this hierarchical structure with Ni and Fe in the outer shell of microspheres facilitates the full exposure of the active sites and facile ion transport kinetics, accounting for remarkable performance towards OER with an overpotential of 239 mV at a current density of 10 mA cm^{-2}. SiO_2, as a sacrificial template, was used for the design of NiFe LDH HMS in the one-step *in situ* growth method. The preparation method is displayed in Fig. 8j. The contact angle tests for NiFe LDH NP (22.5°) and NiFe LDH HMS (0°) with deionized water as the wetting liquid (Fig. 8k) demonstrated improved wettability for the NiFe LDH HMS.[173]

Zheng *et al.*[147] constructed a core–shell structure by the electrodeposition method, which was composed of the NiFe LDH film and the CuO nanorod arrays on Cu foil as the substrate. The obtained core–shell heterostructure exhibited crystalline CuO nanorods as a core and amorphous NiFe LDH as the shell. The TEM images indicated that the NiFe LDH film was uniformly coated on the CuO nanorods, achieving a core–shell heterostructure with a diameter of 300 nm. In 1 M KOH solution, the fabricated catalyst required an OER overpotential of 290 mV to achieve a current density of 50 mA cm^{-2}. The catalyst also achieved a mass activity of 150 A g^{-1} at a low overpotential of 300 mV. The smallest value of charge transfer resistance (0.48 Ω) and the highest value of double-layer capacitance (17 mF cm^{-2}) demonstrated that the faster charge transfer ability and more exposed active sites enhance the performance of the core–shell heterostructure of NiFe LDH/CuO NRs/CF (NRs: nanorods, CF copper foil).[147]

In addition to Cu-incorporated NiFe LDH, Ren and co-workers[179] developed bifunctional 3D core–shell Cu@NiFe LDH catalysts, which exhibited excellent performance towards OER as well HER in 1 M KOH. The facile synthetic approach has been used in the fabrication of self-supported 3D core–shell Cu@NiFe LDH catalyst. The details are given in the schematic illustration (Fig. 9a). Fig. 9b, which depicts that the NiFe LDH nanosheets (NSs) grow vertically on the Cu NWs, provide amply exposed edges. The diameter of the core–shell hybrid was measured to be ~700 nm (~200 nm core of Cu NWs and ~250 nm shell of NiFe LDH NSs). Fig. 9c is the high magnification TEM image of the NiFe LDH NSs with a thickness in the range of 3.2 to 4.0 nm. Such a 3D core–shell nanostructure with few-layer NiFe LDH NSs maximize the surface area and enable more active edge sites to be exposed, thus promoting the catalytic activity. The characteristic lattice fringe with an interplanar spacing of 0.25 nm (inset in Fig. 9c) was recognized, which was assigned to the (012) plane of NiFe LDH. The prepared 3D core–shell Cu@NiFe LDH catalyst has shown enhanced electrocatalytic OER activity (Fig. 9d) with an overpotential of 199 mV at a current density of 10 mA cm^{-2} and HER activity (Fig. 9e) with an overpotential of 116 mV at 10 mA cm^{-2}. The Cu@NiFe LDH electrode also shows a very small Tafel slope of 27.8 mV dec^{-1}, displaying the inherent excellent OER activity as well as good overall water splitting performance with a cell voltage of 1.54 V at 10 mA cm^{-2}.[179] Further, Ren *et al.*[146] observed that amorphous NiFe LDH nanosheets decorated on 3D conductive nickel phosphide nanoarrays exhibit enhanced activity and stability for OER. The integrated 3D core–shell assembly also offers remarkable electrical conductivity for fast ion diffusion, greater surface area with ample active edge sites, and hierarchical nanostructure for the fast release of gas bubbles, hence contributing to the outstanding catalytic performance. In the synthetic process, at first, nickel phosphide nanoarrays were grown on Ni foam by direct phosphorization, followed by electrodeposition of the NiFe LDH nanosheets on the as-prepared nickel phosphide. The observation shows that the NiFe LDH nanosheets were interconnected with each other to form a 3D-ordered network with abundantly exposed edges. The thickness of the whole hybrid micro-sheets was measured to be about 240 nm, which could be tuned by controlling the electrodeposition time. The prepared 3D core–shell electrode achieved high current densities of 300 mA cm^{-2} at extremely low overpotentials of 283 mV and a low Tafel slope of 46.6 mV dec^{-1}. The Ni_5P_4/NiP_2/NiFe LDH hybrid exhibited smaller charge transfer resistance ($R_{ct} = 1.2$ Ω), indicating rapid charge transfer, high-quality electrical integration, and strong contact of the catalysts with the substrates.[146]

In addition, Cu-based foil or foam was used as a carrier owing to its great conductivity to enhance the electrochemical performance of HER and OER. However, due to the limited surface area of Cu-based supports, $Cu(OH)_2$ nano-arrays were always synthesized on the surface to carry the LDH material.[196,207] Cheng *et al.*[196] applied the strategy of developing

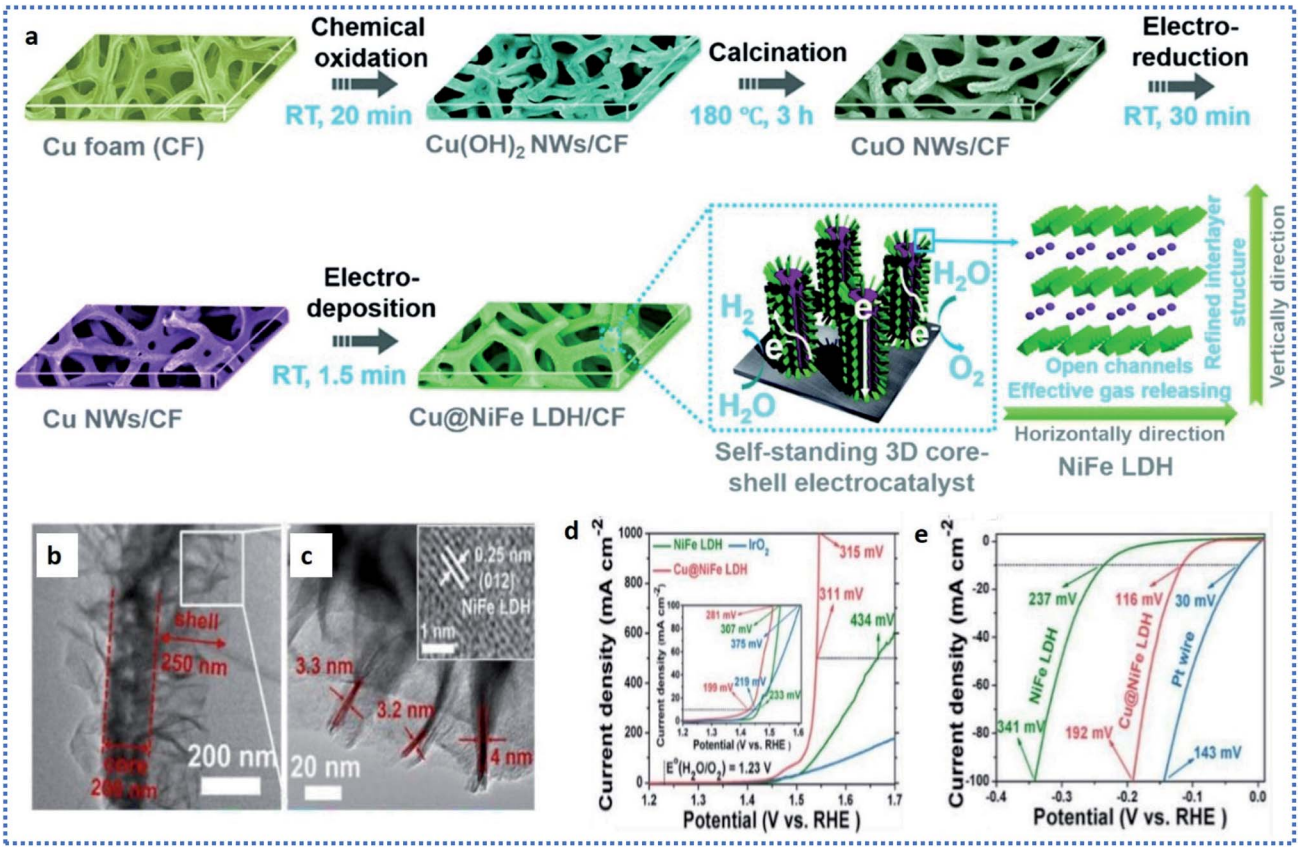

Fig. 9 (a) Schematic illustration of the fabrication procedures of the self-standing 3D core–shell Cu@NiFe LDH electrocatalysts. (b) TEM image of Cu@NiFe LDH. (c) Detailed image of the square part in (b) and HRTEM image of Cu@NiFe LDH to show the lattice fringe (inset). (d) Polarization curves showing the OER performance of Cu@NiFe LDH in 1 M KOH. (e) Polarization curves showing the HER performance of Cu@NiFe LDH in 1 M KOH. Reproduced with permission.[179] Copyright 2017, the Royal Society of Chemistry.

a core–shell structure by growing the Cu_3P nanoarray on Cu foil, which could act as the final carrier to NiFe LDH, by which the poor electrical conductance can be enhanced and the exposure of the active sites could be improved. Cu_3P@NiFe LDH/CF was obtained by morphology-controlled synthesis. At first, $Cu(OH)_2$/CF was synthesized through the oxidation of CF in alkaline media. $Cu(OH)_2$ nanoarray (length of *ca.* 3–8 mm and width of *ca.*100 nm) with a uniform distribution on CF was observed through the SEM images. The ordered Cu_3P nanoarray was obtained *via* the phosphorization process by the addition of a small amount of NaH_2PO_2. Later, this as-obtained Cu_3P/CF was further used as a substrate to carry NiFe LDH through a simple solvothermal method (8 h, 100 °C) to obtain Cu_3P@NiFe LDH/CF. The electrocatalytic study of the catalysts showed the enhanced catalytic performance of Cu_3P@NiFe LDH/CF toward OER (overpotential of 235 mV@10 mA cm^{-2}). The chronopotentiometry (v–t) measurements indicated the highly durable nature of Cu_3P@NiFe LDH/CF.[196]

5.4. Heteroatom doping in the NiFe LDH electrocatalyst

Apart from nanostructuring or hierarchical/core–shell structure designing, heteroatom doping into binary NiFe LDH is also demonstrated to be an effective technique to enhance the performance towards OER and HER.[136,176,208,209] When the NiFe-based oxides are doped with non-metallic heteroatoms (such as P, B, or S), the catalytic role is still the center of the NiFe but the presence of the heteroatoms further tunes the electronic structure around Ni and Fe, which is beneficial to accelerate the charge transport process and may also result in the variation in the oxidation state of Ni in the composites, thereby promoting the water oxidation reaction.[210] Recently, Liu *et al.* found that the exposed O sites on the pristine NiOOH are more catalytically active than the Ni sites and play an imperative part in the OER process.[211] Liu's group has built a series of NiMOOH LDH models with M = Co, Cu, Fe, Mn, Mo, and W and their OER performance was systematically screened by DFT calculations. The volcano plot was constructed based on the theoretical overpotential and $\Delta G_{OOH^*} - \Delta G_{O^*}$ (Fig. 10). The study revealed that Ni@NiFe-2 shows an uncommon performance towards OER with an overpotential of 210 mV and completely outclassed the noble catalysts such as RuO_2 and IrO_2.

Zhu *et al.*[212] designed self-supported ultrathin atomic Cr-doped FeNi-LDH nanosheet arrays on stainless steel (SS) mesh, in which SS acts as a substrate as well as the metal precursor and organic multidentate ligand (2,5-dihydroxybenzenedicarboxylic acid, H_4DOBDC) as a capping agent (Fig. 11a). The average thickness of the peeled nanosheets was

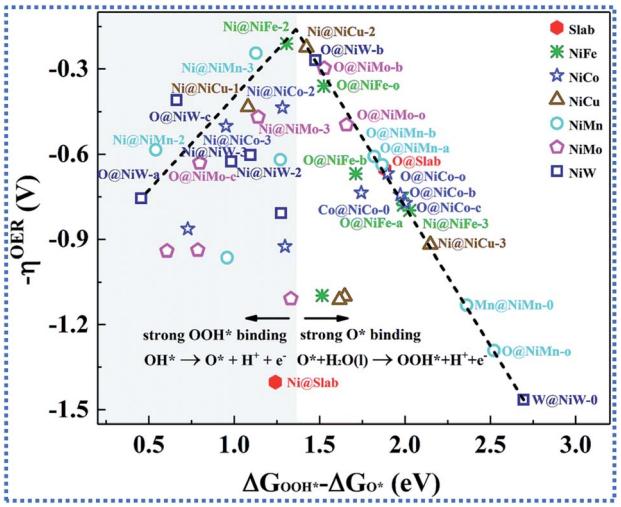

Fig. 10 Calculated overpotential ($-\eta_{OER}$) *vs.* Gibbs free binding energy difference between OOH* and O* at various reaction sites. Reproduced with permission.[211] Copyright 2019, the Royal Society of Chemistry.

found to be 1.69 nm, as measured by atomic force microscopy (AFM) (Fig. 11b). Further, the XAFS and XPS analysis explored the importance of Cr doping. Studies revealed that dominant Cr^{3+} atoms in Cr_1/FeNi-LDH-SS, which possess special electronic configuration of $t_{2g}^3e_g^0$, facilitated electron capture and charge transfer. The as-prepared Cr_1/FeNi-LDH-SS catalyst exhibited outstanding electrochemical OER performance with the overpotentials of 202 mV at the current density of 10 mA cm^{-2} and Tafel slope of 32.5 mV dec^{-1}. The electron-withdrawing characteristic of the Cr^{3+} atoms affected the decrease in the electron densities of the Ni and Fe sites in Cr_1/FeNi-LDH-SS.[212]

Feng *et al.*[130] reported that exceptional performance towards HER was shown by NiFe LDH when doped with Ru. The Ru-doped NiFe LDH nanosheets with a lateral size of 90–180 nm and a thickness of 23 nm were grown *in situ* on nickel foam using a one-pot hydrothermal process (Fig. 11c). The XRD results indicated that the characteristic facets of NiFeRu-LDH with peaks (003), (006), and (009) emerged at 11.6°, 22.6°, and 33.9°, respectively. XPS analysis revealed the oxidation states in the composite as Ni^{2+}, Fe^{3+}, and Ru^{3+}. Remarkably, the prepared NiFeRu-LDH catalyst exhibited excellent HER activity with the

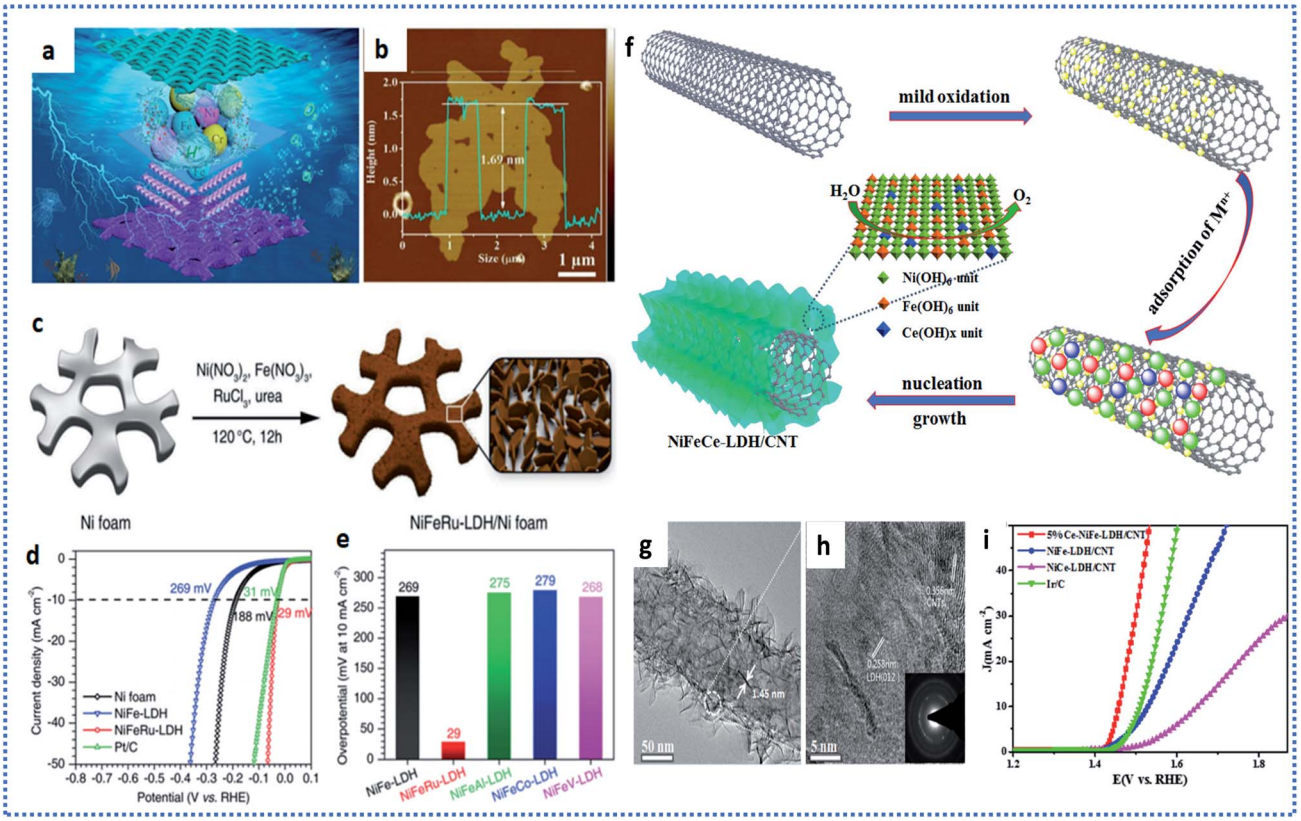

Fig. 11 (a) Schematic diagram. (b) AFM of Cr1/FeNi-LDH-SS or peeled Cr1/FeNi-LDH. Reproduced with permission.[212] Copyright 2020, the Royal Society of Chemistry. (c) Schematic illustration of the *in situ* growth of the NiFeRu-LDH on Ni foam. (d) HER polarization curves of the NiFeRu-LDH, NiFe LDH, Ni-foam, and Pt/C electrocatalysts. (e) The HER overpotentials of the NiFe LDH, NiFeRu-LDH, NiFeAl-LDH, NiFeCo-LDH, and NiFeV-LDH electrocatalysts. Reproduced with permission.[130] Copyright 2018, WILEY-VCH. (f) Assembly of the NiFeCe-LDH/CNT nanocomposite. (g) TEM image. (h) HRTEM image of 5.0% Ce–NiFe LDH/CNT, inset: the corresponding SAED patterns. (i) LSV curves of 5.0% Ce–NiFe LDH/CNT, NiFe LDH/CNT, NiCe-LDH/CNT, and Ir/C catalysts for OER. Reproduced with permission.[183] Copyright 2018, American Chemistry Society.

lowest overpotential of 29 mV (Fig. 11d) at a current density of 10 mA cm^{-2} and a low Tafel slope of 31 mV dec^{-1} in 1 M KOH electrolyte. The group also studied the other metal (Al, Co, and V)-doped NiFe LDH for HER (Fig. 11e). The poor performance of NiFeAl-LDH, NiFeCo-LDH, and NiFeV-LDH could be associated with their weak binding abilities toward hydrogen- and oxygen-containing intermediates.[130]

Besides, earlier studies indicated that optimal Ce doping in the LDH structure can boost the OER and HER catalytic activity by modulating the local chemical binding environment and electronic structure. The modified structure can improve the electronic/ionic conductivity and ion/charge transfer behavior, which ensures plentiful active sites and high oxygen transfer to the reaction sites and strongly promote electrocatalytic water splitting performance with better stability.[183,213] Tang *et al.*[183] developed self-assembled Ce-doped NiFe LDH nanosheets/nanocarbon hierarchical nanocomposite. The prepared NiFeCe-LDH/CNT catalyst exhibited enhanced OER performance owing to its significant structural characteristics along with the high intrinsic catalytic activity, extensive redox properties, and high flexible coordination number of Ce^{3+} and the strongly coupled interface as well. The preparation scheme is illustrated in Fig. 11f. The TEM images revealed that the abundant ultrathin nanosheets are vertically grown on the CNT with the thickness of about 1.45 nm (Fig. 11g and h). The electrochemical testing results in 1 M KOH for OER shows that 5.0% Ce–NiFe LDH/CNT exhibited the lowest overpotential of ~227 mV at a current density of 10 mA cm^{-2} (Fig. 11i).[183] Seo *et al.*[178] performed the electrodeposition process at room temperature and achieved the growth of Ce-doped NiFe LDH on Ni foam. To construct the Ce-doped NiFe LDH, Ce was used to partially replace Fe such that $NiFe_{1-x}Ce_x$, where x varied from 0 to 0.3. The $NiFe_{0.8}Ce_{0.2}$ electrocatalyst exhibited the highest double layer capacitance (4.0 mF cm^{-2}) and ECSA (100 cm^2). The number of active sites was also calculated (14.04×10^{-5} mol) in phosphate buffer solution at pH 7. The electrocatalyst also demonstrated excellent stability for more than 50 hours. Thus, the selection of an appropriate dopant can pave the way for exploring facile, low-cost, and scalable synthesis of novel, highly active electrocatalyst for energy storage and conversion applications.[178]

Moreover, Daniel *et al.*[132] demonstrated highly efficient and stable OER catalyst by the systematic incorporation of cobalt into NiFe LDHs. The cobalt-intercalated NiFe LDH catalyst was prepared by annealing pre-synthesized NiFe LDH at 220 °C for 2 h. Cobalt substitution in NiFe LDH was further explored by the DFT study and the theoretical overpotential was calculated. The LDH structures were simulated and the relaxed structures of the initial and final intermediate states are shown in Fig. 12a. The anticipated density of states (Fig. 12b) indicates that the hybridization of the Co 3d states with O 2p states modifies the density of states close to the valence band maximum (VBM), which successfully changes the bonding strength of O* relative to HO* and HOO*. Fig. 12c depicts the free energy diagram of NiFe LDH, which manifests the rate-limiting step. On the other hand, Fig. 12d and e clearly show that Co doping effectively decreases the free energy difference ΔG_2. Congruently, the overpotential is decreased from 0.82 V to 0.78 V. When practically tested in 1 M KOH, cobalt-intercalated NiFe LDH showed excellent performance towards OER, which exhibited a geometric current density of 10 mA cm^{-2} at a relatively low overpotential of 265 mV (Fig. 12f) and a Tafel slope of only 47 mV dec^{-1} (Fig. 12g).[132]

In addition, doping of other cations/elements, including noble as well as non-noble metals into NiFe LDH such as molybdate-intercalated NiFe LDH nanosheets,[11] ternary NiFeV LDH,[214] S-doped NiFe LDH,[215] $Ni_{0.8}Fe_{0.2}$-m/t-$Se_{0.02}$-LDH,[216] Mn^{2+}-doped NiFe LDH array,[209] Pt–NiFe LDH,[131] NiFeAu LDH,[217] and Ni_3feAl_x-LDH/NF[208] have been shown to enhance the electrocatalytic OER and HER performance towards water splitting.

All the aforementioned design strategies, including the construction of nanostructures, hierarchical core–shell, heteroatom doping or exfoliation, and interlayer ion-exchange, are efficient techniques to engineer NiFe LDH catalyst with hybrid composites and reach active sites, thereby causing discrete performances. The NiFe LDH-based catalysts exhibit low overpotentials, achieve high current densities, and deliver high intrinsic activities. In addition, modified-NiFe LDH with controlled doping can also help to increase the electrical conductivity by reducing the charge transfer resistance. Moreover, thickness regulation of the nanosheets in the layered structure by exfoliation is established to accomplish enhanced performance. Despite the noticeable progress in a highly active NiFe LDH catalyst, the practical applications are still under development. To figure out the potential for scalability, the mass activity and turn over frequency (TOF) need to be evaluated. We survey the mass activity of highly active NiFe LDH-based catalysts and the results are displayed in Fig. 13a. It demonstrates that the high catalyst loading substantially decreases the overpotential value.[146,177,178,191] However, such a high loading of catalyst could restrict their use in industrial applications. Thus, for the catalysts to be industrially applicable, the high mass activity, and low overpotential are of paramount and supreme importance, which could then serve as a potential candidate for scalability.[180,181,218] Similarly, another imperative parameter, which could affect the scalability is, the TOF value. However, it is impossible to establish an analysis of the TOF value due to unavailability of information. Fig. 13b shows the activity trend of NiFe LDH-based catalysts based on the TOF value.[39,152,157,158,208,209,219–222] It could be observed that the ranking of the material (Fig. 11b) is certainly different from that of the catalysts, which exhibited high mass activity (Fig. 13a). Thus, all the NiFe LDH-based catalysts presented here are intrinsically confined by the scaling relations.

6. Bifunctional NiFe LDH-based electrocatalysts for overall water splitting

In practice, water electrolyzers need an active catalyst to facilitate both the reactions, *i.e.*, HER and OER. In addition, using a single OER and HER bifunctional electrocatalyst facilitates the overall system design and drops the cost. Driving the

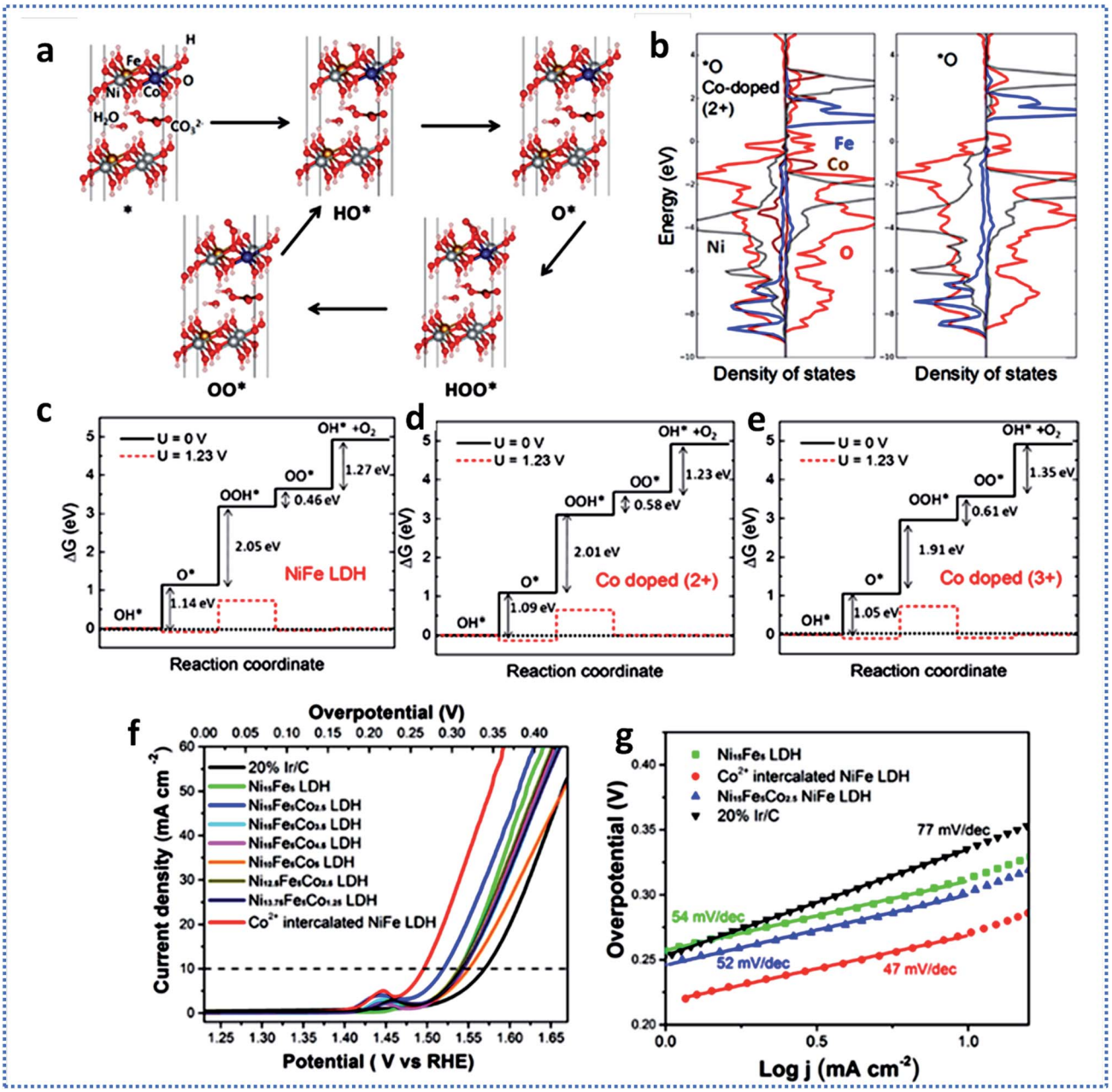

Fig. 12 (a) Relaxed structures of the initial and intermediate states. (b) The projected density of states of oxygen absorbed NiFe LDH (*O) with and without Co doping (in 2+ charge state) in metal hydroxide nanosheets. Standard free energy diagrams for (c) NiFe LDH, (d) Co^{2+}-doped NiFe LDH, (e) Co^{3+}-doped NiFe LDH. (f) Polarization curves showing the electrochemical performance of Co-modified (intercalated and substituted) NiFe LDH, pristine NiFe LDH, and 20% iridium carbon. (g) Tafel plots. Reproduced with permission.[132] Copyright 2018, American Chemistry Society.

electrolyzer with a low cell voltage at the same time to attain high current density is one of the great challenges. Thus, combining the merits of HER and OER electrocatalyst to design durable and efficient OER-HER bifunctional heterostructures that exhibit binding force to both oxygen- and hydrogen-containing intermediates are of tremendous importance for enhancing the activity of overall water splitting. Gao *et al.*[195] reported the bifunctional nature of $NiFe_2O_4$ nanoparticles (dia. 100 nm)/NiFe LDH nanosheets (lateral size 1.5 μm), which has a synergistic effect on their catalytic activities for HER, OER, and overall water splitting (Fig. 14a). With the mass loading of 2.8 mg cm^{-2}, the catalyst required the voltage of 1.535 V to drive in a two-electrode electrolyzer (Fig. 14b) at the current density of 10 mA cm^{-2}. The catalyst with the heterostructure array requires 1.932 V to reach 500 mA cm^{-2} with long-term stability of 20 h (Fig. 14c). The heterostructured catalyst exhibited a faradaic efficiency of 92.6% and plentiful catalytically active sites, greater electronic conductivity, as well as high catalytic

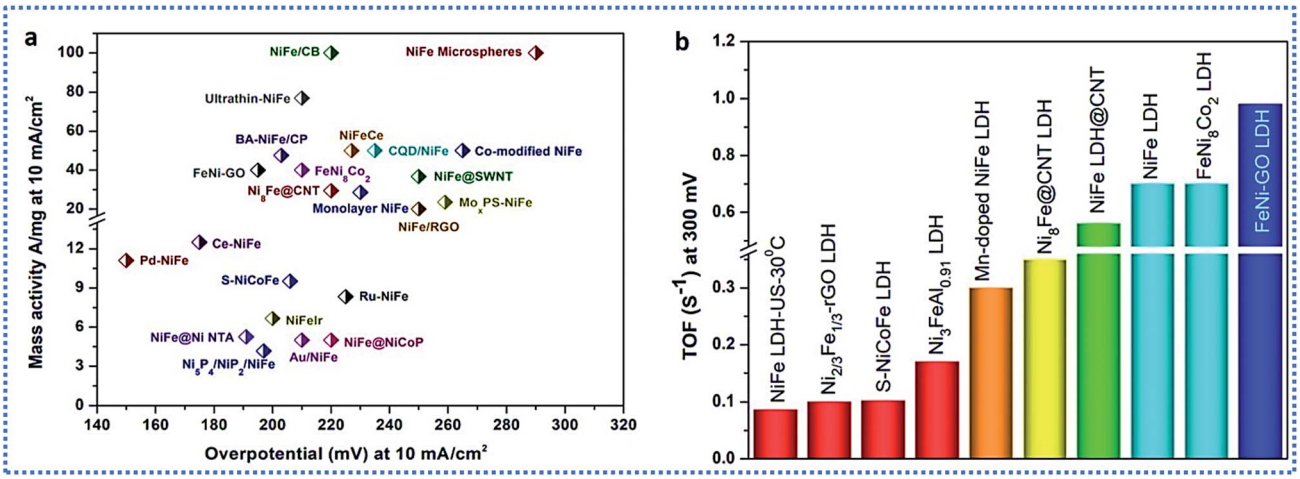

Fig. 13 An overview of NiFe LDH-based electrocatalysts. (a) Mass activity measured at 10 mA cm^{-2} and overpotential for 10 mA cm^{-2} reported in the literature. The presented data were reported originally as follows: Ni_5P_4/NiP_2/NiFe LDH,[146] Au/NiFe LDH,[175] NiFe@Ni NTA LDH,[191] NiFeIr LDH,[176] NiFe@NiCoP LDH,[135] Ru–NiFe LDH,[130] S–NiCoFe LDH,[219] Pd–NiFe LDH,[177] Ce–NiFe LDH,[178] NiFe RGO LDH,[194] Monolayer NiFe LDH,[172] Ni_8Fe@CNT LDH,[220] FeNi-GO LDH,[157] $FeNi_8$ Co_2 LDH,[222] BA–NiFe/CP LDH,[185] NiFeCe LDH,[183] ultrathin–NiFe LDH,[218] NiFe/CB LDH,[180] Mo_x PS–NiFe LDH,[134] NiFe@SWNT LDH,[192] CQD/NiFe LDH,[181] Co-modified NiFe LDH,[132] NiFe-microspheres LDH,[174] and (b) TOF values of NiFe LDH-based electrocatalyst at 300 mV reported in the literature. The presented data were reported originally as follows: NiFe LDH-US-30 °C,[152] $Ni_{2/3}Fe_{1/3}$-rGO LDH,[158] S–NiCoFe LDH,[219] $Ni_3FeAl_{0.91}$ LDH,[208] Mn-doped NiFe LDH,[209] Ni_8Fe@CNT LDH,[220] NiFe LDH@CNT,[39] NiFe LDH,[221] $FeNi_8Co_2$ LDH,[222] FeNi-GO LDH.[157]

reactivity.[195] Li *et al.*[190] designed hierarchical hetero-Ni_3Se_4@-NiFe LDH micro/nanosheets, which served as an efficient bifunctional electrocatalyst for water splitting. The electrocatalyst was prepared on carbon fiber cloth by employing a three-step hydrothermal method. The hierarchical heterostructure assembly displayed improved HER performance with an overpotential of 85 mV and OER performance with an overpotential of 223 mV in 1 M KOH at the current density of 10 mA cm^{-2}. When the catalyst was operated in a two-electrode system in 1 M KOH electrolyte, it acted as an efficient and robust bifunctional electrocatalyst for overall water splitting, which delivered a current density of 10 mA cm^{-2} at a cell potential of 1.54 V (Fig. 14f). The schematic drawing and digital photograph of the electrolytic cell during operation show the formation of H_2 and O_2 bubbles on the cathode and anode, respectively (Fig. 14d and e). The electrocatalyst also remained stable for more than 100 h with negligible decay in the performance (Fig. 14g).[190] Lu *et al.*[223] developed a Ni_2P@$FePo_x$ heterostructure catalyst by extracting Ni from NiFe LDH. During water splitting, the heterostructure was converted to the Ni_2P@NiFe hydroxide heterostructure (P–NiFe), which served as a high performance electrocatalyst for both HER (overpotential of 75 mV) and OER (overpotential of 205 mV) at 10 mA cm^{-2} in 1 M KOH electrolyte. Further, it could attain a stable current density of 10 mA cm^{-2} for overall water splitting at 1.51 V in 1 M KOH with long-term stability of 100 h. A DFT study revealed that the mixed-metal heterostructure of Ni_2P@$NiFeO(OH)_3$ exhibited the lowest ΔG_{H^*} value of 0.06 eV at the catalytic site of Ni, which was closer to the ideal value of zero, indicating higher HER performance. The enhanced OER activity of P–NiFe was also investigated by DFT calculations, which showed that the heterostructure and inclusion of Fe can tune the binding energies of the intermediates, resulting in enhanced OER performance. The LSV measurements for overall splitting (Fig. 14h) indicate that it only requires a cell voltage of 1.51 V to reach a 10 mA cm^{-2} current density in 1 M KOH and show long-term durability of 100 h (Fig. 14i).[223] Zhang *et al.*[135] successfully prepared binder-free 3D hierarchical heterostructure electrode composed of the NiFe LDH@NiCoP nanowires on nickel foam *via* a facile three-step hydrothermal-phosphorization-hydrothermal method (Fig. 14j). The nanowire morphology of NiFe LDH@NiCoP was revealed by the TEM image (Fig. 14k). The fabricated electrocatalyst on nickel foam (NF) required an overpotential of 120 mV for HER and 220 mV for OER at 10 mA cm^{-2} when tested in 1 M KOH electrolyte. As the NiFe LDH@NiCoP/NF served as a high-performance catalyst for both HER and OER, it was also utilized simultaneously as the anode and cathode for full water splitting. The digital photograph of the electrolytic cell during operation is displayed in Fig. 14l. The polarization curves depicted in Fig. 14m indicated that the NiFe LDH@NiCoP/NF exhibited superior overall water splitting activity. The ultra-low cell potential of 1.57 V was required to achieve a current density of 10 mA cm^{-2} and exhibited long-term stability of 100 h (Fig. 14n).[135]

Further, to attain improved bifunctionality of the LDH material for water splitting, various ideas have been developed by the researcher in the past few years.[127,130,223–226] However, to date, the study on the utilization of Pd to enhance the water electrolysis activity of current non-noble-metal catalysts, especially for hydroxides, is still at the nascent stage. For instance, Zhang *et al.*[177] fabricated Pd-decorated NiFe LDH on nickel foam (NF) to achieve improved bifunctionality for water splitting. The hydrothermal synthesis of NiFe LDH flowers on NF, followed by electrodeposition of ultrafine Pd nanoparticles onto

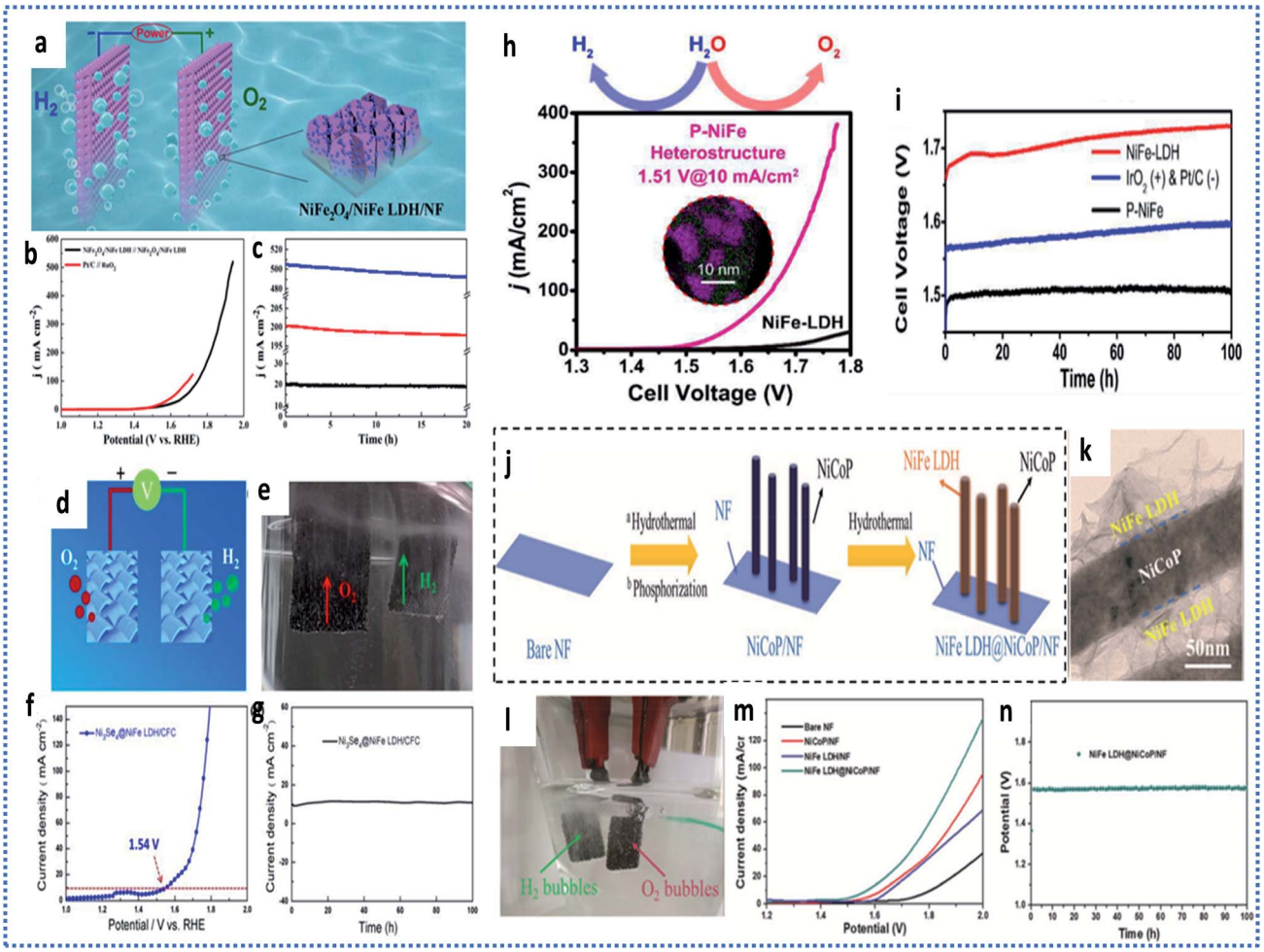

Fig. 14 (a) Schematic illustration. (b) LSV curves of overall water splitting with $NiFe_2O_4$/NiFe LDH||$NiFe_2O_4$/NiFe LDH and RuO_2||Pt/C in the two-electrode configuration. (c) Chronoamperometric measurements of the $NiFe_2O_4$/NiFe LDH||$NiFe_2O_4$/NiFe LDH couple at 1.60, 1.82, and 1.94 V for 20 h, respectively. Reproduced with permission.[195] Copyright 2018, American Chemistry Society. (d) Schematic diagram. (e) Digital photograph of the two-electrode system in which the hierarchical hetero-Ni_3Se_4@NiFe LDH/CFC was used as both the anode and cathode. (f) The LSV polarization curve of Ni_3Se_4@NiFe LDH/CFC//Ni_3Se4@NiFe LDH/CFC. (g) Long term stability test of the hierarchical hetero-Ni_3Se_4@NiFe LDH/CFC for overall water splitting recorded at a current density of 10 mA cm^{-2}. Reproduced with permission.[190] Copyright 2019, the Royal Society of Chemistry. (h) LSV curves of P–NiFe and NiFe LDH as HER and OER bifunctional catalysts in 1 M KOH solution for overall water splitting. (i) Current density traces of CCE at 10 mA cm^{-2} for overall water splitting. Reproduced with permission.[223] Copyright 2018, the Royal Society of Chemistry. (j) Schematic representation of the synthesis of 3D hierarchical NiFe LDH@NiCoP/NF electrodes. (k) TEM image of the NiFe LDH@NiCoP nanowire. (l) Digital photograph of the two-electrode configuration during operation at a constant current density of 100 mA cm^{-2}. (m) Polarization curves of the as-prepared catalysts. (n) Long-term stability test of NiFe LDH@NiCoP/NF for overall water splitting recorded at a current density of 10 mA cm^{-2}. Reproduced with permission.[135] Copyright 2018, WILEY-VCH.

NiFe LDH nanosheets, produced Pd–NiFe LDH/NF. The prepared Pd–NiFe LDH showed the flowerlike morphology, which was formed with nanosheet subunits (thickness 500 to 2000 nm). The as-obtained Pd–NiFe LDH/NF exhibited a remarkably improved activity when it was subjected to the OER test (overpotential of 235 mV@10 mA cm^{-2}). The Pd–NiFe LDH/NF electrode was also evaluated for HER in 1 M KOH and showed much improved HER activity, achieving low overpotential of 130 mV@10 mA cm^{-2}. The bifunctionality of Pd–NiFe LDH/NF was investigated for overall water splitting in a two-electrode system. The ultra-low cell potential of 1.514 V was required to achieve current densities of 10 mA cm^{-2}. The chronoamperometric test indicated satisfactory stability (30 h) of the bifunctional Pd–NiFe LDH/NF electrode @20 mA cm^{-2}.[177]

In addition, Chen *et al.*[169] applied self-growing strategy to fabricate hierarchical-structure NiFe LDH nanosheets on Ni nanowires (NWs). Initially, Ni NWs were utilized as the Ni source and the catalyst skeleton, and after a fast and well-controlled redox reaction with the iron(III) salt, the coprecipitation process generated the NiFe LDH NS shell around the conductive Ni NW core. This unique core–shell structure overcomes the problem of low conductivity in the conventional LDH film. Owing to their desirable compositions and unique structural advantages, the as-prepared NiFe LDH NSs manifested improved electrocatalytic activity toward alkaline water

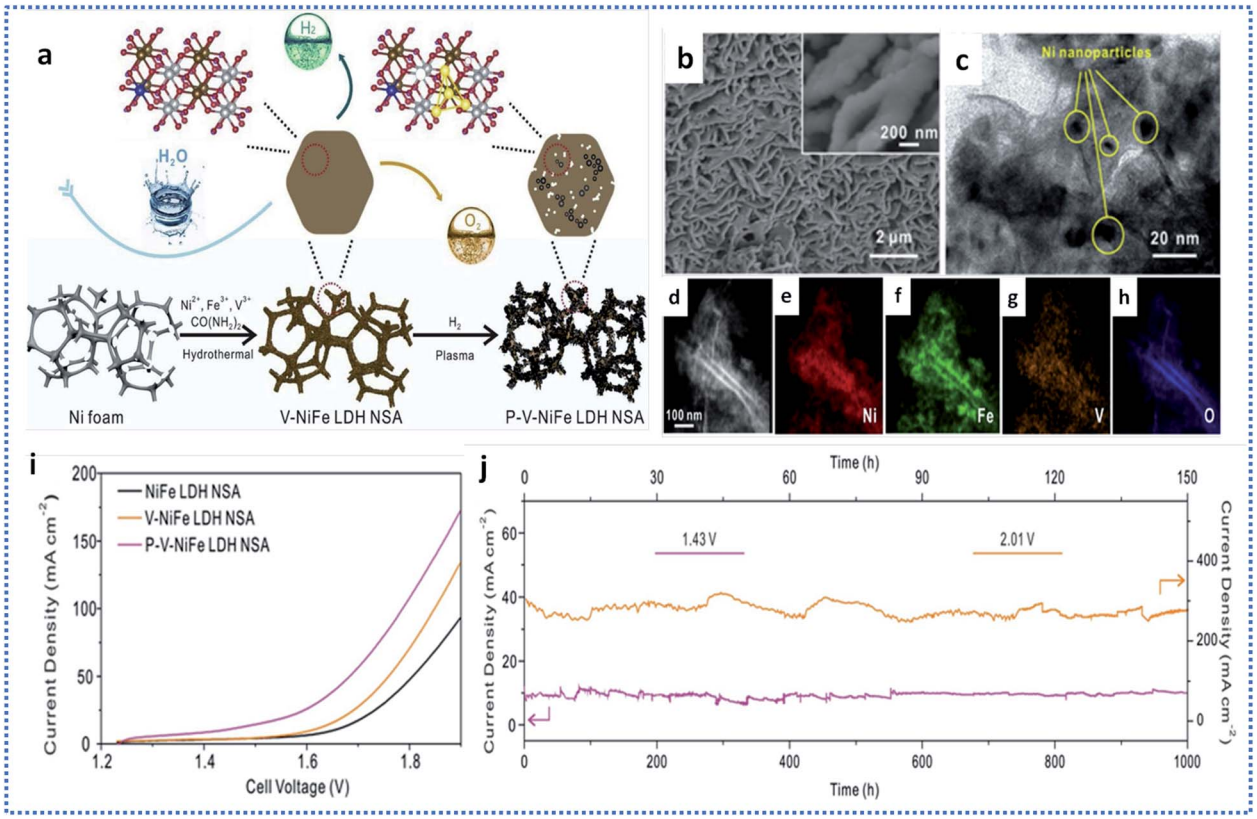

Fig. 15 (a) Schematic illustration of the fabrication process of P–V–NiFe LDH NSA. (b) SEM image. (c) TEM image. (d–h) HAAF-STEM and corresponding elemental mapping images of P–V–NiFe LDH NSA. (i) Overall water splitting performance of NiFe LDH, V–NiFe LDH NSA, and P–V–NiFe LDH NSA. (j) CA tests at 1.43 V for P–V–NiFe NSA. Reproduced with permission.[227] Copyright 2020, Elsevier.

oxidation. This catalyst performed as a superior OER electrocatalyst and exhibited a low onset overpotential of 230 mV at 10 mA cm^{-2} owing to its unique composition and hierarchical NS@NW structure with the conductive Ni NW core as the electron channel. Further, the NiFe LDH NSs was converted to Fe-doped Ni_2P nanosheets (Fe–Ni_2P NSs) or Fe-doped $NiSe_2$ nanosheets ($FeNiSe_2$ NSs) upon phosphorization or selenization treatments, which also showed enhanced HER performance in 1 M KOH solution. The overall water splitting performance of the alkaline electrolyzer was evaluated in the two-electrode configuration using NiFe LDH NSs as the anode and Fe–Ni_2P NSs or Fe–$NiSe_2$ NSs as the cathode, respectively, which can afford a current density of 30 mA cm^{-2} at a cell voltage of 1.69 and 1.76 V, respectively, with excellent long-term durability.[169]

Recently, Yu *et al.*[227] reported outstanding performance towards HER by cation-doped NiFe LDH. A heterostructure with Ni nanoparticles anchored on oxygen and nickel vacancy-rich V-doped NiFe LDH nanosheets were constructed by applying the doping and H_2 plasma reduction strategy (Fig. 15a). The SEM image (Fig. 15b) reveals the nanosheet morphology, while the nanoparticles anchored on the nanosheets could be observed by TEM image (Fig. 15c). The HAAF-STEM and elemental mapping images of the P–V–NiFe LDH NSA is shown in Fig. 15d–h, indicating the homogeneous distribution of constituent elements throughout the prepared catalyst. The synthesized electrocatalyst exhibited an exceptionally high performance towards HER in 1 M KOH with the lowest overpotential of 19 mV @10 mA cm^{-2} and small Tafel slope of 38 mV dec^{-1}. Further, when tested as a bifunctional electrocatalyst for overall water splitting (Fig. 15i), a small cell voltage (1.43 V at 10 mA cm^{-2}) and ultra-long stability (over 1000 h) were achieved (Fig. 15j). Density functional theory (DFT) calculations exposed that V doping, oxygen vacancy, Ni vacancy, and Ni nanoparticles were responsible for improving the conductivity. The V-doping and oxygen vacancy can efficiently reduce the energy barrier of O* in OER and the Ni/NiFe LDH heterostructure ameliorates the electronic structure and tunes the electron transfer rate.[227]

Besides, other NiFe LDH-based bifunctional electrocatalysts including Mo–Ni_2P@NiFe LDH/NF, CoFe@NiFe LDH/NF, and CoSe@NiFe LDH/NF have shown excellent performance for overall water splitting with good durability.[228–230] Fig. 16 depicts the comparison of the overall water splitting cell voltage and stability for NiFe LDH-based bifunctional electrocatalyst. An important note to consider while observing Fig. 16 is to recognize the NiFe LDH-based catalyst that could serve as the best bifunctional candidate, which operates at a low cell potential and shows greater stability for overall water splitting in order to work as a commercial electrolyzer. Several NiFe LDH-based catalysts have shown the best performance in terms of requirement of low cell potential towards overall water splitting; however, the durability is still an issue. For overall water splitting or practical application, the potential candidate,

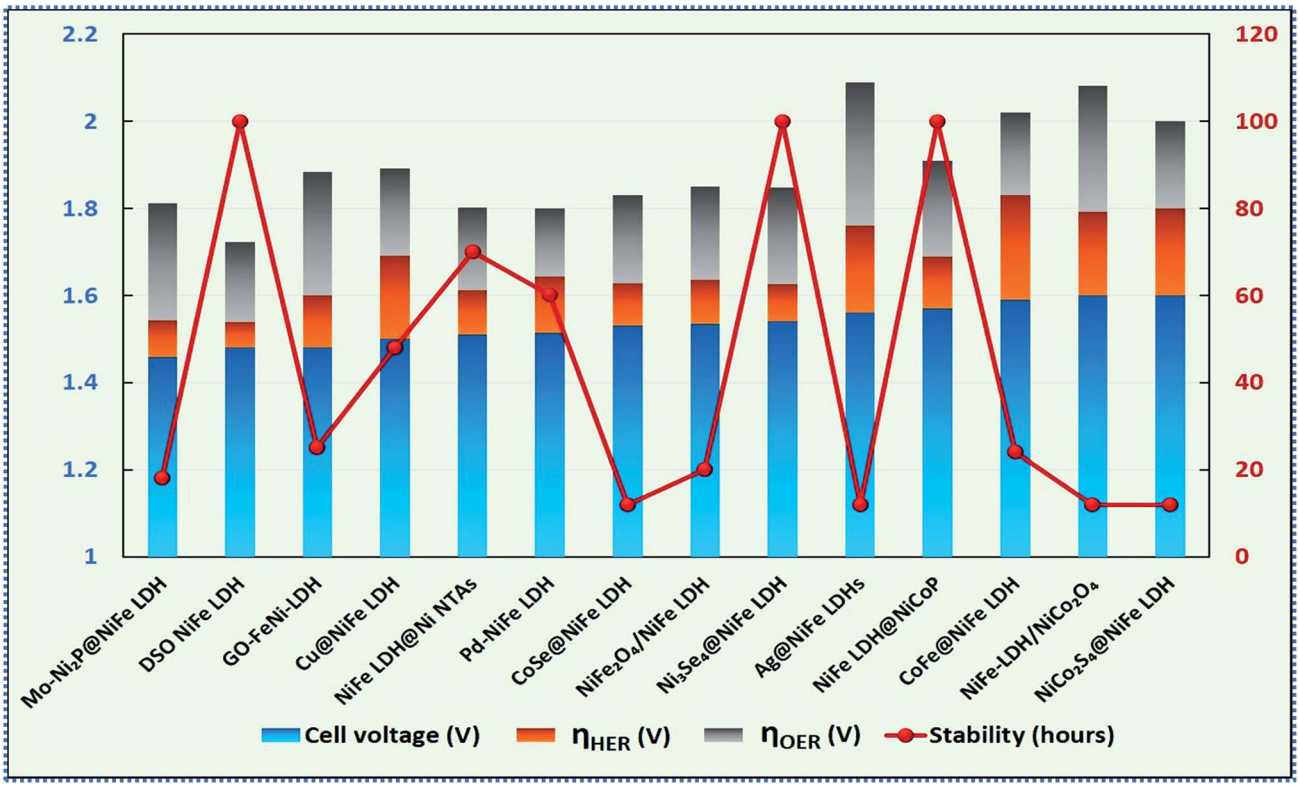

Fig. 16 Overview of the overall water splitting cell voltage and stability for NiFe LDH-based bifunctional electrocatalyst. The presented data were originally reported as follows: Mo–Ni_2P@NiFe LDH,[228] DSO NiFe LDH,[127] GO-FeNi-LDH,[188] Cu@NiFe LDH,[179] NiFe LDH@Ni NTAs,[191] Pd–NiFe LDH,[177] CoSe@NiFe LDH,[229] $NiFe_2O_4$/NiFe LDH,[195] Ni_3Se_4@NiFe LDH,[190] Ag@NiFe LDHs,[140] NiFe LDH@NiCoP,[135] CoFe@NiFe LDH,[230] NiFe LDH/$NiCo_2O_4$,[133] $NiCo_2S_4$@NiFe LDH.[138]

considering both performance and durability, is the DSO NiFe LDH catalyst (Fig. 16). Thus, the design of promising bifunctional and highly durable catalysts, which can be integrated into renewable technologies, remains a challenge.

7. Conclusion and future outlook

The electrolysis of water is considered to be one of the most sustainable and effective ways to produce hydrogen. Over the past few decades, continuous efforts have been devoted to the design, modification, and application of non-noble electrocatalyst for water splitting. This review endeavors to sum up the systematic overview of the recent progress, current status, and novel achievements of NiFe LDH-based catalysts for electrochemical water splitting. We comprehensively surveyed the promising results of pristine and hybrid NiFe LDH-based electrocatalysts. The catalysts exhibited excellent OER and HER performance in alkaline solution owing to their flexible electronic structure, tunable 2D lamellar structure, and chemical composition. However, poor intrinsic activity and inadequate active sites are the foremost two critical variables influencing the electrocatalytic activity of NiFe LDH materials and restricting their large-scale application. More precisely, this review explores the recent advancement in terms of design regulation, physicochemical properties, density functional theory calculations, and electrocatalytic performances on various hierarchical/core–shell nanostructured NiFe LDH-based catalysts including interlayer anion exchanged NiFe LDH, exfoliated NiFe LDH, and heteroatom-doped NiFe LDH. Later, the bifunctional performance of NiFe LDH-based catalysts for overall water splitting is also provided. Even though NiFe LDH-based electrocatalysts have drawn substantial attention because of their great abundance and easy accessibility, there is still room for performance improvements. To enhance the performance of NiFe LDH-based electrocatalysts for use in a practical water electrolyzer system, the following options should be considered:

(i) Regulating the interlayer distance and type of intercalation anion in the interlayer region in the NiFe LDH-based material could widen the accessible surface areas of the NiFe LDH-based electrocatalysts and effectively promote charge transfer. Such sorts of intercalated anions could also modulate the surface electronic structure of an active species, thereby enhancing the intrinsic catalytic activity of the active sites.

(ii) Although NiFe LDH-based hierarchical core–shell nanostructures have recorded extraordinary signs of progress in electrochemical water splitting, several challenges remain. From the viewpoint of novel material exploration, it is still alluring to fabricate NiFe LDH with well-defined structure and tunable properties. In the progression of electrocatalysis of NiFe LDH, some major challenges include abridging the exfoliation process with the precise control of layer thickness, adequate exposure of the active sites, and long-term catalytic stability. Moreover, in the existing phase of a bifunctional catalyst advancement for water splitting, the understanding of the reaction mechanism *via*

theoretical prediction is lacking. Besides, the tunable unique layered structure offers more opportunities for facilitating novel NiFe LDH catalyst for the water splitting.

(iii) Constructing multi-hybrid NiFe LDH-based electrocatalysts is considered to be a powerful strategy for further enhancing the efficiency of electrochemical water splitting. The multi-hybrid nanostructures of the NiFe LDH-based catalysts could facilitate the electron transfer and improve the performance of electrocatalytic water splitting.

(iv) Heteroatom doping has also been investigated as an alternative and effective method for the enhancement of catalytic performance for NiFe LDH-based catalysts. Heteroatom doping could alter the electronic structure and morphology in terms of size and thickness, which can improve the electrical conductivity and enhance the kinetic reaction, which also assists in increasing the intrinsic catalytic activity. Thus, heteroatom-doped NiFe LDH-based electrocatalysts can further enhance and modulate the catalytic activity for water splitting.

(v) In the current stage of NiFe LDH-based bifunctional catalysts, the development of electrochemical water splitting, *in situ* spectroscopic investigations, and theoretical prediction needs to be addressed. Understanding the specific mechanism of HER and OER of NiFe LDH-based bifunctional electrocatalysts by modifying the electronic and crystal structure *via* theoretical and experimental study could provide useful guidance towards the design of efficient bifunctional NiFe LDH-based electrocatalysts.

Although, NiFe LDH is a class of low-cost non-noble material, the factors that affect the scale-up relation need to be addressed. The intrinsic activity of the catalyst is of foremost importance compared to the geometric activity.[231] TOF, considered as an activity metric for scalability, need to be evaluated. A robust and highly durable electrocatalyst, which could require the lowest overpotential simultaneously to achieve high current density, is yet to discover. Most such investigate themes have not yet been examined and will be anticipated within the near future. We expect that this review can provide an insightful outline to the readers.

In summary, the present review has provided in-depth understanding on the design, fabrication, and performance of the NiFe electrocatalyst, particularly through morphology engineering, constructing hierarchical/core–shell nanostructures, and doping heteroatoms. The recent progresses in the bifunctional activity of the NiFe LDH catalyst for overall water splitting suggests that the NiFe-based catalyst could play a vital role in electrolyzers at the industrial level.

Conflicts of interest

The authors declare no competing financial interest.

Acknowledgements

Pradnya Bodhankar and Pradip Sarawade acknowledge WOS-A scheme (SR/WOS-A/PM-9/2018(G)) under DST for their financial support.

References

1 N. S. Lewis and D. G. Nocera, *Proc. Natl. Acad. Sci. U.S.A.*, 2006, **103**, 15729–15735.
2 M. Dresselhaus and I. Thomas, *Nature*, 2001, **414**, 332–337.
3 J. O. M. Bockris and T. N. Veziroglu, *Int. J. Hydrogen Energy*, 2007, **32**, 1605–1610.
4 W. Yang, Z. Wang, W. Zhang and S. Guo, *Trends Chem.*, 2019, **1**, 259–271.
5 B. You and Y. Sun, *Acc. Chem. Res.*, 2018, **51**, 1571–1580.
6 B. Xiong, L. Chen and J. Shi, *ACS Catal.*, 2018, **8**, 3688–3707.
7 S. Anantharaj, P. E. Karthik, B. Subramanian and S. Kundu, *ACS Catal.*, 2016, **6**, 4660–4672.
8 W. Hu, Y. Wang, X. Hu, Y. Zhou and S. Chen, *J. Mater. Chem.*, 2012, **22**, 6010–6016.
9 Y. Lee, J. Suntivich, K. J. May, E. E. Perry and Y. Shao-Horn, *J. Phys. Chem. Lett.*, 2012, **3**, 399–404.
10 K. A. Stoerzinger, O. Diaz-Morales, M. Kolb, R. R. Rao, R. Frydendal, L. Qiao, X. R. Wang, N. B. Halck, J. Rossmeisl and H. A. Hansen, *ACS Energy Lett.*, 2017, **2**, 876–881.
11 Y. Jin, H. Wang, J. Li, X. Yue, Y. Han, P. K. Shen and Y. Cui, *Adv. Mater.*, 2016, **28**, 3785–3790.
12 H. Wang, H.-W. Lee, Y. Deng, Z. Lu, P.-C. Hsu, Y. Liu, D. Lin and Y. Cui, *Nat. Commun.*, 2015, **6**, 1–8.
13 X. Zou and Y. Zhang, *Chem. Soc. Rev.*, 2015, **44**, 5148–5180.
14 J. Wang, F. Xu, H. Jin, Y. Chen and Y. Wang, *Adv. Mater.*, 2017, **29**, 1605838.
15 L. Wu, Q. Li, C. H. Wu, H. Zhu, A. Mendoza-Garcia, B. Shen, J. Guo and S. Sun, *J. Am. Chem. Soc.*, 2015, **137**, 7071–7074.
16 Y. Zhao, X. Jia, G. Chen, L. Shang, G. I. Waterhouse, L.-Z. Wu, C.-H. Tung, D. O'Hare and T. Zhang, *J. Am. Chem. Soc.*, 2016, **138**, 6517–6524.
17 J. Su, J. Zhou, L. Wang, C. Liu and Y. Chen, *Sci. Bull.*, 2017, **62**, 633–644.
18 M.-R. Gao, J.-X. Liang, Y.-R. Zheng, Y.-F. Xu, J. Jiang, Q. Gao, J. Li and S.-H. Yu, *Nat. Commun.*, 2015, **6**, 1–7.
19 H. Yan, C. Tian, L. Wang, A. Wu, M. Meng, L. Zhao and H. Fu, *Angew. Chem., Int. Ed.*, 2015, **54**, 6325–6329.
20 M. Shalom, D. Ressnig, X. Yang, G. Clavel, T. P. Fellinger and M. Antonietti, *J. Mater. Chem. A*, 2015, **3**, 8171–8177.
21 A. Chunduri, S. Gupta, O. Bapat, A. Bhide, R. Fernandes, M. Patel, V. Bambole, A. Miotello and N. Patel, *Appl. Catal. B Environ.*, 2019, **259**, 118051.
22 Y. Li, B. Huang, Y. Sun, M. Luo, Y. Yang, Y. Qin, L. Wang, C. Li, F. Lv and W. Zhang, *Small*, 2019, **15**, 1804212.
23 W. Hao, R. Wu, R. Zhang, Y. Ha, Z. Chen, L. Wang, Y. Yang, X. Ma, D. Sun and F. Fang, *Adv. Energy Mater.*, 2018, **8**, 1801372.
24 P. Babar, A. Lokhande, H. H. Shin, B. Pawar, M. G. Gang, S. Pawar and J. H. Kim, *Small*, 2018, **14**, 1702568.
25 L. Chen, X. Dong, Y. Wang and Y. Xia, *Nat. Commun.*, 2016, **7**, 1–8.
26 H. Jin, J. Wang, D. Su, Z. Wei, Z. Pang and Y. Wang, *J. Am. Chem. Soc.*, 2015, **137**, 2688–2694.

27 D. S. Dhawale, P. Bodhankar, N. Sonawane and P. B. Sarawade, *Sustainable Energy Fuels*, 2019, **3**, 1713–1719.
28 Z. Lu, W. Xu, W. Zhu, Q. Yang, X. Lei, J. Liu, Y. Li, X. Sun and X. Duan, *Chem. Commun.*, 2014, **50**, 6479–6482.
29 L. Lv, Z. Yang, K. Chen, C. Wang and Y. Xiong, *Adv. Energy Mater.*, 2019, **9**, 1803358.
30 E. Nurlaela, T. Shinagawa, M. Qureshi, D. S. Dhawale and K. Takanabe, *ACS Catal.*, 2016, **6**, 1713–1722.
31 Y. Wang, D. Yan, S. El Hankari, Y. Zou and S. Wang, *Adv. Sci.*, 2018, **5**, 1800064.
32 S. Anantharaj, K. Karthick and S. Kundu, *Mater. Today Energy*, 2017, **6**, 1–26.
33 Q. Wang and D. O'Hare, *Chem. Rev.*, 2012, **112**, 4124–4155.
34 M. A. Oliver-Tolentino, J. Vázquez-Samperio, A. Manzo-Robledo, R. D. G. Gonzalez-Huerta, J. L. Flores-Moreno, D. Ramírez-Rosales and A. Guzmán-Vargas, *J. Phys. Chem. C*, 2014, **118**, 22432–22438.
35 A. Malak-Polaczyk, C. Vix-Guterl and E. Frackowiak, *Energy Fuel.*, 2010, **24**, 3346–3351.
36 F. Song and X. Hu, *J. Am. Chem. Soc.*, 2014, **136**, 16481–16484.
37 X. Ge, C. Gu, X. Wang and J. Tu, *J. Mater. Chem. A*, 2014, **2**, 17066–17076.
38 Y. Vlamidis, E. Scavetta, M. Gazzano and D. Tonelli, *Electrochim. Acta*, 2016, **188**, 653–660.
39 M. Gong, Y. Li, H. Wang, Y. Liang, J. Z. Wu, J. Zhou, J. Wang, T. Regier, F. Wei and H. Dai, *J. Am. Chem. Soc.*, 2013, **135**, 8452–8455.
40 L. Dang, H. Liang, J. Zhuo, B. K. Lamb, H. Sheng, Y. Yang and S. Jin, *Chem. Mater.*, 2018, **30**, 4321–4330.
41 X. Zou, A. Goswami and T. Asefa, *J. Am. Chem. Soc.*, 2013, **135**, 17242–17245.
42 C. Qiao, Y. Zhang, Y. Zhu, C. Cao, X. Bao and J. Xu, *J. Mater. Chem. A*, 2015, **3**, 6878–6883.
43 W. Liu, J. Bao, M. Guan, Y. Zhao, J. Lian, J. Qiu, L. Xu, Y. Huang, J. Qian and H. Li, *Dalton Trans.*, 2017, **46**, 8372–8376.
44 L. Feng, A. Li, Y. Li, J. Liu, L. Wang, L. Huang, Y. Wang and X. Ge, *ChemPlusChem*, 2017, **82**, 483–488.
45 F. Song and X. Hu, *Nat. Commun.*, 2014, **5**, 1–9.
46 L. Trotochaud, S. L. Young, J. K. Ranney and S. W. Boettcher, *J. Am. Chem. Soc.*, 2014, **136**, 6744–6753.
47 J. Qi, W. Zhang, R. Xiang, K. Liu, H. Y. Wang, M. Chen, Y. Han and R. Cao, *Adv. Sci.*, 2015, **2**, 1500199.
48 W. Zhang, J. Qi, K. Liu and R. Cao, *Adv. Energy Mater.*, 2016, **6**, 1502489.
49 B. M. Hunter, W. Hieringer, J. Winkler, H. Gray and A. Müller, *Energy Environ. Sci.*, 2016, **9**, 1734–1743.
50 R. Subbaraman, D. Tripkovic, K.-C. Chang, D. Strmcnik, A. P. Paulikas, P. Hirunsit, M. Chan, J. Greeley, V. Stamenkovic and N. M. Markovic, *Nat. Mater.*, 2012, **11**, 550–557.
51 L. Trotochaud, J. K. Ranney, K. N. Williams and S. W. Boettcher, *J. Am. Chem. Soc.*, 2012, **134**, 17253–17261.
52 Z. Cai, X. Bu, P. Wang, J. C. Ho, J. Yang and X. Wang, *J. Mater. Chem. A*, 2019, **7**, 5069–5089.
53 G. B. B. Varadwaj and V. O. Nyamori, *Nano Res.*, 2016, **9**, 3598–3621.
54 L. Zhou, M. Shao, M. Wei and X. Duan, *J. Energy Chem.*, 2017, **26**, 1094–1106.
55 C. Tang, H. F. Wang, X. L. Zhu, B. Q. Li and Q. Zhang, *Part. Part. Syst. Char.*, 2016, **33**, 473–486.
56 R. Allmann, *Acta Crystallogr. Sect. B Struct. Crystallogr. Cryst. Chem.*, 1968, **24**, 972–977.
57 H. Taylor, *Mineral. Mag.*, 1969, **37**, 338–342.
58 H. Taylor, *Mineral. Mag.*, 1969, **37**, 338–385.
59 G. Mishra, B. Dash and S. Pandey, *Appl. Clay Sci.*, 2018, **153**, 172–186.
60 C. Forano, U. Costantino, V. Prévot and C. T. Gueho, in *Developments in clay science*, Elsevier, 2013, vol. 5, pp. 745–782.
61 A. I. Khan and D. O'Hare, *J. Mater. Chem.*, 2002, **12**, 3191–3198.
62 M. Shao, R. Zhang, Z. Li, M. Wei, D. G. Evans and X. Duan, *Chem. Commun.*, 2015, **51**, 15880–15893.
63 X. Long, Z. Wang, S. Xiao, Y. An and S. Yang, *Mater. Today*, 2016, **19**, 213–226.
64 Y. Shabangoli, M. S. Rahmanifar, M. F. El-Kady, A. Noori, M. F. Mousavi and R. B. Kaner, *Energy Storage Materials*, 2018, **11**, 282–293.
65 R. Patel, J. T. Park, M. Patel, J. K. Dash, E. B. Gowd, R. Karpoormath, A. Mishra, J. Kwak and J. H. Kim, *J. Mater. Chem. A*, 2018, **6**, 12–29.
66 Y. Jia, L. Zhang, G. Gao, H. Chen, B. Wang, J. Zhou, M. T. Soo, M. Hong, X. Yan and G. Qian, *Adv. Mater.*, 2017, **29**, 1700017.
67 C. Yu, Z. Liu, X. Han, H. Huang, C. Zhao, J. Yang and J. Qiu, *Carbon*, 2016, **110**, 1–7.
68 Y. Wang, C. Xie, Z. Zhang, D. Liu, R. Chen and S. Wang, *Adv. Funct. Mater.*, 2018, **28**, 1703363.
69 N. Han, F. Zhao and Y. Li, *J. Mater. Chem. A*, 2015, **3**, 16348–16353.
70 J. Bockris, B. Dandapani, D. Cocke and J. Ghoroghchian, *Int. J. Hydrogen Energy*, 1985, **10**, 179–201.
71 M. Sastri, *Hydrogen energy progress IX : proceedings of the 9th World Hydrogen Energy Conference*, ed. T. N. Veziroğlu, C. Derive and J. Pottier, Paris, France, 22-25 June 1992.
72 A. Venugopal, S. N. Kumar, J. Ashok, D. H. Prasad, V. D. Kumari, K. Prasad and M. Subrahmanyam, *Int. J. Hydrogen Energy*, 2007, **32**, 1782–1788.
73 M. Oertel, J. Schmitz, W. Weirich, D. Jendryssek-Neumann and R. Schulten, *Chem. Eng. Technol.*, 1987, **10**, 248–255.
74 S. K. Liu, *US Pat.*, USOO5958365A, 1999.
75 V. Hacker, R. Fankhauser, G. Faleschini, H. Fuchs, K. Friedrich, M. Muhr and K. Kordesch, *J. Power Sources*, 2000, **86**, 531–535.
76 T. E. Dowdy, *US Pat.*, US005955039A, 1999.
77 J. E. Funk, *Int. J. Hydrogen Energy*, 2001, **26**, 185–190.
78 A. A. Ismail and D. W. Bahnemann, *Sol. Energy Mater. Sol. Cells*, 2014, **128**, 85–101.
79 R. Van de Krol and M. Grätzel, *Photoelectrochemical hydrogen production*, Springer, 2012.

80 R. C. Prince and H. S. Kheshgi, *Crit. Rev. Microbiol.*, 2005, **31**, 19–31.
81 S. Anantharaj, S. R. Ede, K. Sakthikumar, K. Karthick, S. Mishra and S. Kundu, *ACS Catal.*, 2016, **6**, 8069–8097.
82 R. Farrauto, S. Hwang, L. Shore, W. Ruettinger, J. Lampert, T. Giroux, Y. Liu and O. Ilinich, *Annu. Rev. Mater. Res.*, 2003, **33**, 1–27.
83 C. Song, *Catal. Today*, 2002, **77**, 17–49.
84 A. P. Simpson and A. E. Lutz, *Int. J. Hydrogen Energy*, 2007, **32**, 4811–4820.
85 D. K. Liguras, D. I. Kondarides and X. E. Verykios, *Appl. Catal. B Environ.*, 2003, **43**, 345–354.
86 N. V. Gnanapragasam, B. V. Reddy and M. A. Rosen, *Int. J. Hydrogen Energy*, 2010, **35**, 4933–4943.
87 J. Dempsey, *Module 2: Hydrogen Use*, 2001.
88 T. Hisatomi, J. Kubota and K. Domen, *Chem. Soc. Rev.*, 2014, **43**, 7520–7535.
89 D. Hall, *J. Electrochem. Soc.*, 1981, **128**, 740.
90 H. Wendt and G. Imarisio, *J. Appl. Electrochem.*, 1988, **18**, 1–14.
91 B. You, M. T. Tang, C. Tsai, F. Abild-Pedersen, X. Zheng and H. Li, *Adv. Mater.*, 2019, **31**, 1807001.
92 Y. Matsumoto and E. Sato, *Mater. Chem. Phys.*, 1986, **14**, 397–426.
93 J. O. M. Bockris, *J. Chem. Phys.*, 1956, **24**, 817–827.
94 J. O. M. Bockris and T. Otagawa, *J. Electrochem. Soc.*, 1984, **131**, 290.
95 F. Gutmann and O. J. Murphy, in *Modern aspects of electrochemistry*, Springer, 1983, pp. 1–82.
96 E. Fabbri, A. Habereder, K. Waltar, R. Kötz and T. J. Schmidt, *Catal. Sci. Technol.*, 2014, **4**, 3800–3821.
97 J. M. Bockris and E. Potter, *J. Electrochem. Soc.*, 1952, **99**, 169–186.
98 R. Parsons, *Trans. Faraday Soc.*, 1958, **54**, 1053–1063.
99 J. K. Nørskov, T. Bligaard, A. Logadottir, J. Kitchin, J. G. Chen, S. Pandelov and U. Stimming, *J. Electrochem. Soc.*, 2005, **152**, J23–J26.
100 J. F. Callejas, C. G. Read, C. W. Roske, N. S. Lewis and R. E. Schaak, *Chem. Mater.*, 2016, **28**, 6017–6044.
101 Z. Guo, J. Zhou and Z. Sun, *J. Mater. Chem. A*, 2017, **5**, 23530–23535.
102 Y. Zhang, B. Ouyang, K. Xu, X. Xia, Z. Zhang, R. S. Rawat and H. J. Fan, *Small*, 2018, **14**, 1800340.
103 A. T. Landers, M. Fields, D. A. Torelli, J. Xiao, T. R. Hellstern, S. A. Francis, C. Tsai, J. Kibsgaard, N. S. Lewis and K. Chan, *ACS Energy Lett.*, 2018, **3**, 1450–1457.
104 H. Dau, C. Limberg, T. Reier, M. Risch, S. Roggan and P. Strasser, *ChemCatChem*, 2010, **2**, 724–761.
105 A. J. Bard, L. R. Faulkner, J. Leddy and C. G. Zoski, *Electrochemical methods: fundamentals and applications*, Wiley, New York, 1980.
106 J. O. M. Bockris, *Fundamental aspects of electrocrystallization*, Springer Science & Business Media, 2012.
107 L. Wu, L. Yu, X. Xiao, F. Zhang, S. Song, S. Chen and Z. Ren, *Research*, 2020, **2020**, 3976278.
108 J. Tafel, *Z. Phys. Chem.*, 1905, **50**, 641–712.
109 G. Burstein, *Corros. Sci.*, 2005, **47**, 2858–2870.
110 I. Hartung, S. Kirsch, P. Zihrul, O. Müller and T. von Unwerth, *J. Power Sources*, 2016, **307**, 280–288.
111 C. C. McCrory, S. Jung, J. C. Peters and T. F. Jaramillo, *J. Am. Chem. Soc.*, 2013, **135**, 16977–16987.
112 N.-U.-A. Babar and K. S. Joya, *ACS Omega*, 2020, **5**, 10651–10662.
113 S. Wang, J. Wu, J. Yin, Q. Hu, D. Geng and L. M. Liu, *ChemElectroChem*, 2018, **5**, 1357–1363.
114 L. Yu, J. F. Yang, B. Y. Guan, Y. Lu and X. W. Lou, *Angew. Chem., Int. Ed.*, 2018, **57**, 172–176.
115 D. Zhou, Z. Cai, Y. Bi, W. Tian, M. Luo, Q. Zhang, Q. Xie, J. Wang, Y. Li and Y. Kuang, *Nano Res.*, 2018, **11**, 1358–1368.
116 M. Gong and H. Dai, *Nano Res.*, 2015, **8**, 23–39.
117 T. A. Edison, *US Pat.*, 876 445, 1908.
118 D. A. Corrigan, *J. Electrochem. Soc.*, 1987, **134**, 377–384.
119 D. Corrigan and R. Bendert, 1988.
120 B. M. Hunter, J. R. Winkler and H. B. Gray, *Molecules*, 2018, **23**, 903.
121 B. M. Hunter, N. B. Thompson, A. M. Müller, G. R. Rossman, M. G. Hill, J. R. Winkler and H. B. Gray, *Joule*, 2018, **2**, 747–763.
122 C. Feng, M. B. Faheem, J. Fu, Y. Xiao, C. Li and Y. Li, *ACS Catal.*, 2020, **10**, 4019–4047.
123 N. Li, D. K. Bediako, R. G. Hadt, D. Hayes, T. J. Kempa, F. Von Cube, D. C. Bell, L. X. Chen and D. G. Nocera, *Proc. Natl. Acad. Sci. U.S.A.*, 2017, **114**, 1486–1491.
124 B. J. Trześniewski, O. Diaz-Morales, D. A. Vermaas, A. Longo, W. Bras, M. T. Koper and W. A. Smith, *J. Am. Chem. Soc.*, 2015, **137**, 15112–15121.
125 M. Görlin, P. Chernev, J. Ferreira de Araújo, T. Reier, S. r. Dresp, B. Paul, R. Krähnert, H. Dau and P. Strasser, *J. Am. Chem. Soc.*, 2016, **138**, 5603–5614.
126 Z. Cai, D. Zhou, M. Wang, S. M. Bak, Y. Wu, Z. Wu, Y. Tian, X. Xiong, Y. Li and W. Liu, *Angew. Chem.*, 2018, **130**, 9536–9540.
127 Z. Qiu, C.-W. Tai, G. A. Niklasson and T. Edvinsson, *Energy Environ. Sci.*, 2019, **12**, 572–581.
128 J. Y. Chen, L. Dang, H. Liang, W. Bi, J. B. Gerken, S. Jin, E. E. Alp and S. S. Stahl, *J. Am. Chem. Soc.*, 2015, **137**, 15090–15093.
129 Y. Gu, Y. Wang, W. An, Y. Men, Y. Rui, X. Fan and B. Li, *New J. Chem.*, 2019, **43**, 6555–6562.
130 G. Chen, T. Wang, J. Zhang, P. Liu, H. Sun, X. Zhuang, M. Chen and X. Feng, *Adv. Mater.*, 2018, **30**, 1706279.
131 W. Zhu, L. Liu, Z. Yue, W. Zhang, X. Yue, J. Wang, S. Yu, L. Wang and J. Wang, *ACS Appl. Mater. Interfaces*, 2017, **9**, 19807–19814.
132 A. C. Thenuwara, N. H. Attanayake, J. Yu, J. P. Perdew, E. J. Elzinga, Q. Yan and D. R. Strongin, *J. Phys. Chem. B*, 2018, **122**, 847–854.
133 Z. Wang, S. Zeng, W. Liu, X. Wang, Q. Li, Z. Zhao and F. Geng, *ACS Appl. Mater. Interfaces*, 2017, **9**, 1488–1495.
134 Y.-Y. Dong, D.-D. Ma, X.-T. Wu and Q.-L. Zhu, *Inorg. Chem. Front.*, 2020, **7**, 270–276.

135 H. Zhang, X. Li, A. Hähnel, V. Naumann, C. Lin, S. Azimi, S. L. Schweizer, A. W. Maijenburg and R. B. Wehrspohn, *Adv. Funct. Mater.*, 2018, **28**, 1706847.
136 S. Anantharaj, K. Karthick, M. Venkatesh, T. V. Simha, A. S. Salunke, L. Ma, H. Liang and S. Kundu, *Nano Energy*, 2017, **39**, 30–43.
137 Q. Yang, T. Li, Z. Lu, X. Sun and J. Liu, *Nanoscale*, 2014, **6**, 11789–11794.
138 J. Liu, J. Wang, B. Zhang, Y. Ruan, L. Lv, X. Ji, K. Xu, L. Miao and J. Jiang, *ACS Appl. Mater. Interfaces*, 2017, **9**, 15364–15372.
139 H.-Y. Si, Q.-X. Deng, L.-C. Chen, L. Wang, X.-Y. Liu, W.-S. Wu, Y.-H. Zhang, J.-M. Zhou and H.-L. Zhang, *J. Alloys Compd.*, 2019, **794**, 261–267.
140 X. Zhang, A. Marianov, Y. Jiang, C. Cazorla and D. Chu, *ACS Appl. Nano Mater.*, 2020, **3**, 887–895.
141 E. L. Crepaldi, P. C. Pavan and J. B. Valim, *J. Braz. Chem. Soc.*, 2000, **11**, 64–70.
142 R. Chen, G. Sun, C. Yang, L. Zhang, J. Miao, H. Tao, H. Yang, J. Chen, P. Chen and B. Liu, *Nanoscale Horiz.*, 2016, **1**, 156–160.
143 H. Qi, J. Wolfe, D. Fichou and Z. Chen, *Sci. Rep.*, 2016, **6**, 30882.
144 Z. Chen, Y. Ha, H. Jia, X. Yan, M. Chen, M. Liu and R. Wu, *Adv. Energy Mater.*, 2019, **9**, 1803918.
145 Z. Xing, L. Gan, J. Wang and X. Yang, *J. Mater. Chem. A*, 2017, **5**, 7744–7748.
146 L. Yu, H. Zhou, J. Sun, I. K. Mishra, D. Luo, F. Yu, Y. Yu, S. Chen and Z. Ren, *J. Mater. Chem. A*, 2018, **6**, 13619–13623.
147 Q. Zhou, T.-T. Li, J. Qian, W. Xu, Y. Hu and Y.-Q. Zheng, *ACS Appl. Energy Mater.*, 2018, **1**, 1364–1373.
148 H. Wang, T. Zhou, P. Li, Z. Cao, W. Xi, Y. Zhao and Y. Ding, *ACS Sustainable Chem. Eng.*, 2018, **6**, 380–388.
149 L. Zhang, R. Zhang, R. Ge, X. Ren, S. Hao, F. Xie, F. Qu, Z. Liu, G. Du and A. M. Asiri, *Chem.–Eur J.*, 2017, **23**, 11499–11503.
150 T. Zhan, X. Liu, S. Lu and W. Hou, *Appl. Catal. B Environ.*, 2017, **205**, 551–558.
151 R. A. Senthil, J. Pan, X. Yang and Y. Sun, *Int. J. Hydrogen Energy*, 2018, **43**, 21824–21834.
152 X. Li, X. Hao, Z. Wang, A. Abudula and G. Guan, *J. Power Sources*, 2017, **347**, 193–200.
153 S. Miyata, *Clay Clay Miner.*, 1983, **31**, 305–311.
154 Z. Liu, R. Ma, M. Osada, N. Iyi, Y. Ebina, K. Takada and T. Sasaki, *J. Am. Chem. Soc.*, 2006, **128**, 4872–4880.
155 N. Iyi, K. Okamoto, Y. Kaneko and T. Matsumoto, *Chem. Lett.*, 2005, **34**, 932–933.
156 N. Iyi, T. Matsumoto, Y. Kaneko and K. Kitamura, *Chem. Mater.*, 2004, **16**, 2926–2932.
157 X. Long, J. Li, S. Xiao, K. Yan, Z. Wang, H. Chen and S. Yang, *Angew. Chem., Int. Ed.*, 2014, **53**, 7584–7588.
158 W. Ma, R. Ma, C. Wang, J. Liang, X. Liu, K. Zhou and T. Sasaki, *ACS Nano*, 2015, **9**, 1977–1984.
159 C. Chen, L. Tao, S. Du, W. Chen, Y. Wang, Y. Zou and S. Wang, *Adv. Funct. Mater.*, 2020, **30**, 1909832–1909849.
160 Y. Wang, Y. Zhang, Z. Liu, C. Xie, S. Feng, D. Liu, M. Shao and S. Wang, *Angew. Chem., Int. Ed.*, 2017, **56**, 5867–5871.
161 L. Li, R. Ma, Y. Ebina, N. Iyi and T. Sasaki, *Chem. Mater.*, 2005, **17**, 4386–4391.
162 W. Hou, L. Kang, R. Sun and Z.-H. Liu, *Colloid. Surface. Physicochem. Eng. Aspect.*, 2008, **312**, 92–98.
163 M. Adachi-Pagano, C. Forano and J.-P. Besse, *Chem. Commun.*, 2000, 91–92.
164 M. a. Jobbágy and A. E. Regazzoni, *J. Colloid Interface Sci.*, 2004, **275**, 345–348.
165 Y. Wei, F. Li and L. Liu, *RSC Adv.*, 2014, **4**, 18044–18051.
166 B. Chen, Z. Zhang, S. Kim, S. Lee, J. Lee, W. Kim and K. Yong, *ACS Appl. Mater. Interfaces*, 2018, **10**, 44518–44526.
167 J. Shen, P. Zhang, R. Xie, L. Chen, M. Li, J. Li, B. Ji, Z. Hu, J. Li and L. Song, *ACS Appl. Mater. Interfaces*, 2019, **11**, 13545–13556.
168 J. Xie, H. Qu, F. Lei, X. Peng, W. Liu, L. Gao, P. Hao, G. Cui and B. Tang, *J. Mater. Chem. A*, 2018, **6**, 16121–16129.
169 X. Teng, L. Guo, L. Ji, J. Wang, Y. Niu, Z. Hu and Z. Chen, *ACS Appl. Energy Mater.*, 2019, **2**, 5465–5471.
170 R. Chen, S. F. Hung, D. Zhou, J. Gao, C. Yang, H. Tao, H. B. Yang, L. Zhang, L. Zhang and Q. Xiong, *Adv. Mater.*, 2019, **31**, 1903909.
171 K. Huang, R. Dong, C. Wang, W. Li, H. Sun and B. Geng, *ACS Sustainable Chem. Eng.*, 2019, **7**, 15073–15079.
172 X. Zhang, Y. Zhao, Y. Zhao, R. Shi, G. I. Waterhouse and T. Zhang, *Adv. Energy Mater.*, 2019, **9**, 1900881.
173 C. Zhang, M. Shao, L. Zhou, Z. Li, K. Xiao and M. Wei, *ACS Appl. Mater. Interfaces*, 2016, **8**, 33697–33703.
174 H. Zhong, T. Liu, S. Zhang, D. Li, P. Tang, N. Alonso-Vante and Y. Feng, *J. Energy Chem.*, 2019, **33**, 130–137.
175 J. Zhang, J. Liu, L. Xi, Y. Yu, N. Chen, S. Sun, W. Wang, K. M. Lange and B. Zhang, *J. Am. Chem. Soc.*, 2018, **140**, 3876–3879.
176 Q.-Q. Chen, C.-C. Hou, C.-J. Wang, X. Yang, R. Shi and Y. Chen, *Chem. Commun.*, 2018, **54**, 6400–6403.
177 J. Guo, J. Sun, Y. Sun, Q. Liu and X. Zhang, *Mater. Chem. Front.*, 2019, **3**, 842–850.
178 H. S. Jadhav, A. Roy, B. Z. Desalegan and J. G. Seo, *Sustainable Energy Fuels*, 2020, **4**, 312–323.
179 L. Yu, H. Zhou, J. Sun, F. Qin, F. Yu, J. Bao, Y. Yu, S. Chen and Z. Ren, *Energy Environ. Sci.*, 2017, **10**, 1820–1827.
180 T. S. Munonde, H. Zheng and P. N. Nomngongo, *Ultrason. Sonochem.*, 2019, **59**, 104716.
181 D. Tang, J. Liu, X. Wu, R. Liu, X. Han, Y. Han, H. Huang, Y. Liu and Z. Kang, *ACS Appl. Mater. Interfaces*, 2014, **6**, 7918–7925.
182 R. Li, J. Xu, J. Ba, Y. Li, C. Liang and T. Tang, *Int. J. Hydrogen Energy*, 2018, **43**, 7956–7963.
183 H. Xu, B. Wang, C. Shan, P. Xi, W. Liu and Y. Tang, *ACS Appl. Mater. Interfaces*, 2018, **10**, 6336–6345.
184 J. Zhou, L. Yu, Q. Zhu, C. Huang and Y. Yu, *J. Mater. Chem. A*, 2019, **7**, 18118–18125.
185 Z. Sun, Y. Wang, L. Lin, M. Yuan, H. Jiang, R. Long, S. Ge, C. Nan, H. Li and G. Sun, *Chem. Commun.*, 2019, **55**, 1334–1337.
186 S. Sirisomboonchai, S. Li, A. Yoshida, X. Li, C. Samart, A. Abudula and G. Guan, *ACS Sustainable Chem. Eng.*, 2018, **7**, 2327–2334.

187 G. Shi, C. Yu, Z. Fan, J. Li and M. Yuan, *ACS Appl. Mater. Interfaces*, 2018, **11**, 2662–2669.
188 X. Han, N. Suo, C. Chen, Z. Lin, Z. Dou, X. He and L. Cui, *Int. J. Hydrogen Energy*, 2019, **44**, 29876–29888.
189 L. Ren, C. Wang, W. Li, R. Dong, H. Sun, N. Liu and B. Geng, *Electrochim. Acta*, 2019, **318**, 42–50.
190 T. Zhang, L. Hang, Y. Sun, D. Men, X. Li, L. Wen, X. Lyu and Y. Li, *Nanoscale Horiz.*, 2019, **4**, 1132–1138.
191 D. Li, G. Hao, W. Guo, G. Liu, J. Li and Q. Zhao, *J. Power Sources*, 2020, **448**, 227434.
192 H. Liu, J. Zhou, C. Wu, C. Wang, Y. Zhang, D. Liu, Y. Lin, H. Jiang and L. Song, *ACS Sustainable Chem. Eng.*, 2018, **6**, 2911–2915.
193 X. Li, H. Wu, Y. Wu, Z. Kou, S. J. Pennycook and J. Wang, *ACS Appl. Nano Mater.*, 2018, **2**, 325–333.
194 T. Zhan, Y. Zhang, X. Liu, S. Lu and W. Hou, *J. Power Sources*, 2016, **333**, 53–60.
195 Z. Wu, Z. Zou, J. Huang and F. Gao, *ACS Appl. Mater. Interfaces*, 2018, **10**, 26283–26292.
196 P. Zhao, H. Nie, Z. Zhou, J. Wang and G. Cheng, *ChemistrySelect*, 2018, **3**, 8064–8069.
197 S. Dutta, A. Indra, Y. Feng, T. Song and U. Paik, *ACS Appl. Mater. Interfaces*, 2017, **9**, 33766–33774.
198 W. Xu, Z. Lu, P. Wan, Y. Kuang and X. Sun, *Small*, 2016, **12**, 2492–2498.
199 X. Liu, X. Wang, X. Yuan, W. Dong and F. Huang, *J. Mater. Chem. A*, 2016, **4**, 167–172.
200 W. Zhang and K. Zhou, *Small*, 2017, **13**, 1700806.
201 D. Deng, K. Novoselov, Q. Fu, N. Zheng, Z. Tian and X. Bao, *Nat. Nanotechnol.*, 2016, **11**, 218.
202 Y. Zhao, X. Zhang, X. Jia, G. I. Waterhouse, R. Shi, X. Zhang, F. Zhan, Y. Tao, L. Z. Wu and C. H. Tung, *Adv. Energy Mater.*, 2018, **8**, 1703585.
203 H. Zhang, H. Li, B. Akram and X. Wang, *Nano Res.*, 2019, **12**, 1327–1331.
204 R. Li, J. Xu, Q. Pan, J. Ba, T. Tang and W. Luo, *ChemistryOpen*, 2019, **8**, 1027–1032.
205 M. Fang, G. Dong, R. Wei and J. C. Ho, *Adv. Energy Mater.*, 2017, **7**, 1700559.
206 J. Mohammed-Ibrahim, *J. Power Sources*, 2019, 227375.
207 X. Jiang, Y. Li, M. He, L. Zhou, Q. Zheng, F. Xie, W. Jie and D. Lin, *Int. J. Hydrogen Energy*, 2019, **44**, 19986–19994.
208 H. Liu, Y. Wang, X. Lu, Y. Hu, G. Zhu, R. Chen, L. Ma, H. Zhu, Z. Tie and J. Liu, *Nano Energy*, 2017, **35**, 350–357.
209 D. Zhou, Z. Cai, Y. Jia, X. Xiong, Q. Xie, S. Wang, Y. Zhang, W. Liu, H. Duan and X. Sun, *Nanoscale Horiz.*, 2018, **3**, 532–537.
210 C. Xuan, J. Wang, W. Xia, J. Zhu, Z. Peng, K. Xia, W. Xiao, H. L. Xin and D. Wang, *J. Mater. Chem. A*, 2018, **6**, 7062–7069.
211 Z. Xue, X. Zhang, J. Qin and R. Liu, *J. Mater. Chem. A*, 2019, **7**, 23091–23097.
212 X. Xie, C. Cao, W. Wei, S. Zhou, X.-T. Wu and Q.-L. Zhu, *Nanoscale*, 2020, **12**, 5817–5823.
213 Q. Zhang, S. Zhang, Y. Tian and S. Zhan, *ACS Sustainable Chem. Eng.*, 2018, **6**, 15411–15418.
214 P. Li, X. Duan, Y. Kuang, Y. Li, G. Zhang, W. Liu and X. Sun, *Adv. Energy Mater.*, 2018, **8**, 1703341.
215 S. Li, J. Liu, S. Duan, T. Wang and Q. Li, *Chin. J. Catal.*, 2020, **41**, 847–852.
216 S. Duan, S. Chen, T. Wang, S. Li, J. Liu, J. Liang, H. Xie, J. Han, S. Jiao and R. Cao, *Nanoscale*, 2019, **11**, 17376–17383.
217 X.-P. Li, W.-K. Han, K. Xiao, T. Ouyang, N. Li, F. Peng and Z.-Q. Liu, *Catal. Sci. Technol.*, 2020, **10**, 4184–4190.
218 C. Kuai, Y. Zhang, D. Wu, D. Sokaras, L. Mu, S. Spence, D. Nordlund, F. Lin and X.-W. Du, *ACS Catal.*, 2019, **9**, 6027–6032.
219 L.-M. Cao, J.-W. Wang, D.-C. Zhong and T.-B. Lu, *J. Mater. Chem. A*, 2018, **6**, 3224–3230.
220 D. Zhao, K. Jiang, Y. Pi and X. Huang, *ChemCatChem*, 2017, **9**, 84–88.
221 Y. Dong, S. Komarneni, F. Zhang, N. Wang, M. Terrones, W. Hu and W. Huang, *Appl. Catal. B Environ.*, 2020, **263**, 118343.
222 X. Long, S. Xiao, Z. Wang, X. Zheng and S. Yang, *Chem. Commun.*, 2015, **51**, 1120–1123.
223 F.-S. Zhang, J.-W. Wang, J. Luo, R.-R. Liu, Z.-M. Zhang, C.-T. He and T.-B. Lu, *Chem. Sci.*, 2018, **9**, 1375–1384.
224 X. Jia, Y. Zhao, G. Chen, L. Shang, R. Shi, X. Kang, G. I. Waterhouse, L. Z. Wu, C. H. Tung and T. Zhang, *Adv. Energy Mater.*, 2016, **6**, 1502585.
225 L. Hui, Y. Xue, B. Huang, H. Yu, C. Zhang, D. Zhang, D. Jia, Y. Zhao, Y. Li and H. Liu, *Nat. Commun.*, 2018, **9**, 1–11.
226 D. Wang, Q. Li, C. Han, Q. Lu, Z. Xing and X. Yang, *Nat. Commun.*, 2019, **10**, 1–12.
227 Y. Tang, Q. Liu, L. Dong, H. B. Wu and X.-Y. Yu, *Appl. Catal. B Environ.*, 2020, 118627.
228 Z. Yang, Y. Lin, F. Jiao, J. Li, J. Wang and Y. Gong, *J. Energy Chem.*, 2020, **49**, 189–197.
229 H. Sun, J.-G. Li, L. Lv, Z. Li, X. Ao, C. Xu, X. Xue, G. Hong and C. Wang, *J. Power Sources*, 2019, **425**, 138–146.
230 R. Yang, Y. Zhou, Y. Xing, D. Li, D. Jiang, M. Chen, W. Shi and S. Yuan, *Appl. Catal. B Environ.*, 2019, **253**, 131–139.
231 J. Kibsgaard and I. Chorkendorff, *Nat. Energy*, 2019, **4**, 430.

